Development of a Femtosecond Cr:ZnSe Seed Laser for Regenerative Amplification

by

Melisa Natali Çizmeciyan

A Thesis Submitted to the
Graduate School of Engineering
in Partial Fulfillment of the Requirements for
the Degree of

Master of Science
in
Materials Science and Engineering

Koç University

August 2009

Koç University
Graduate School of Sciences and Engineering

This is to certify that I have examined this copy of a master's thesis by

Melisa Natali Çizmeciyan

and have found that it is complete and satisfactory in all respects,
and that any and all revisions required by the final
examining committee have been made.

Committee Members:

_____
Alphan Sennaroğlu, Ph. D. (Advisor)

_____
Alper Kiraz, Ph. D.

_____
Kaan Güven, Ph. D.

Date: _____

ABSTRACT

In this thesis work, we describe the three main components of a chirped pulse amplifier (CPA). It is a technique in which nano-joule pulse energies of femtosecond lasers are amplified to micro-joule or milli-joule levels. In particular, the seed laser was experimentally constructed and the numerical design of the stretcher and compressor was completed. The seed laser is a continuous-wave, Kerr-lens mode-locked femtosecond Cr^{2+}:ZnSe laser pumped by a 1800-nm thulium fiber laser. The astigmatically compensated, asymmetric x-cavity contained a 2.4-mm-long Cr^{2+}:ZnSe sample with a pump absorption coefficient of 11.6 cm^{-1}, and it was terminated with a 1% output coupler. Dispersion compensation was achieved by using a MgF_2 prism pair. During Kerr-lens mode-locked operation, the laser generated 95-fs pulses at a pulse repetition rate of 94.3 MHz and with 40 mW of output power. The center wavelength of the pulses was 2.42 μm. The pulses had a spectral width of 69 nm and a time-bandwidth product of 0.335, which is close to the transform limit for hyperbolic secant shaped pulses. In addition, by using the soliton area theorem, the nonlinear refractive index was estimated as 1.4×10^{-14} cm^2/W for Cr^{2+}:ZnSe. The calculated value agrees well with what has been reported in the literature and it is almost 100 times larger than the nonlinear refractive index of sapphire. In the case of the stretcher and compressor design, based on our numerical calculations, the stretcher allows us to stretch 100fs pulses to 100ps by using a diffraction grating pair with a groove density of 300 grooves/mm and separation of 76 cm.

ÖZET

Bu tezde, bir genişletilmiş darbe yükselticisinin elemanları olan çekirdek laseri ile genişletici ve sıkıştırıcı kırınım ağı tasarımı anlatılmıştır. Çekirdek laseri sürekli Kerr kip kilitleme yöntemi ile çalışan bir Cr^{2+}:ZnSe laseridir. Pompa olarak 1800 nm'de çalışan bir tulyum fiber laseri kullanılmıştır. Astigmatik olarak düzeltilmiş x şeklindeki rezonatör içerisindeki 2.4mm uzunluğundaki kristal, Brewster açısında konumlandırılmıştır. Rezonatör %1 geçirgenliğe sahip bir ayna ile sonlandırılmıştır. Kristalin pompa dalgaboyundaki soğurma katsayısı 11.6 cm^{-1} olarak belirlenmiştir. Rezonatör içersindeki fazladan dispersiyonu yoketmek için magnezyum florürden (MgF_2) yapılmış bir çift prizma kullanılmıştır. Laserden 95 fs genişliğine sahip, 94.3 MHz tekrar frekansında darbeler üretilmiştir ve çıkış gücü de 40mW olarak ölçülmüştür. Üretilen darbelerin merkez dalgaboyu 2.42 μm olarak belirlenmiştir ve spektrum genişliği 69nm'ye ulaşmıştır. Eğer üretilen darbelerin hiperbolik sekant dağılımı gösterdiğini varsayarsak, bant genişlik çarpımı 0.335 olarak hesaplandı. Bu, ideal değer olan 0.315'e, yakın bir ölçüdür. Ayrıca, soliton alan teoremi kullanılarak kazanç ortamının dogrusal olmayan kırılma indisi $1.4x10^{-14}$ cm^2/W olarak hesaplandı. Hesaplanan değer literatür değerleri ile örtüşmektedir. Üretilen darbelerin yüseltilmesi sırasında, yükseltici sisteme zarar vermemesi için genişletilmesi gerekmektedir. Bu sebeple 100fs süreli darbeleri 100ps mertebelerine genişletebilen bir genişletici tasarlanmıştır. Bu tasarımda 76 cm aralıklı kırınım ağı çifti kullanılması öngörülmüştür.

ACKNOWLEDGEMENTS

During this thesis work, lots of people put their effort other than me. This part of my thesis is dedicated to them, in order to honor their support. In this sense, I would like to bring up couple of names beginning with my thesis advisor Alphan Sennaroğlu. He offered me a great chance to prove myself in the laboratory, also kept me motivated during my studies in Koç University. He was always doing the best for our benefit, and willing to help whenever we needed.

I was very lucky to interact with Adnan Kurt and Hüseyin Çankaya as well. They helped me without questioning, and fed me with their valuable lab experience continuously. Without their support it would be harder to complete this thesis work.

Kaan Güven and Alper Kiraz deserve special thanks as my thesis committee members. Their valuable comments developed new ideas about this thesis as future work.

Last but not least, my lab friends. In particular, Ümit Demirbaş, Hamit Kalaycıoğlu and Arif Mostafazadeh have inspired me in research, and through our discussions in the lab.

In addition, I also would like to mention my family members beginning with Vania Uluç. We had shared the same destiny with her without knowing it, so talking about our related research topics became a very exciting habit for both of us when she was here.

With no hesitation, my parents Aret, Ani Cizmeciyan, and my sister Lora Cizmeciyan have been providing me with the greatest support and encouragement during at all stages of my education up today whenever I needed.

Nurhan Sözüdoğru kept me motivated and alive while I was doing all the hard work.

Finally, this work has been generously sponsored by Tübitak under the project 108T028 titled “Development of a High-Energy, Cr^{2+}:ZnSe Laser Pulse Amplifier at 2400 nm”.

Table of Content

List of Tables

List of Figures

Nomenclature

σ_a: Absorption cross-section
β: Angle of diffraction
α: Angle of incidence
ω: Angular frequency
ω_0: Beam waist spotsize
τ_C: Cavity photon lifetime
λ_0: Central wavelength
β: Chirp parameter
L_C: Crystal length
τ_D: Delay time
A_{eff}: Effective area
E: Electric field amplitude
σ_e: Emission cross-section
N_2: Excited state population density
τ_f: Final pulsewidth
η_A: Fractional absorbed power
ν_P: Frequency of pump photons
ν_L: Frequency of laser photons
g: Gain
g_D: Groove density
N_1: Ground state population density
D: Group velocity dispersion (GVD)
τ_0: Initial pulsewidth
δ: Kerr coefficient
ω_L: Laser beam waist
L_G: Optical path between two gratings
φ_0: Phase
v_P: Phase velocity
h: Planck's constant
ΔN: Population inversion
P: Power
S: Pointing vector
W: Pulse energy
τ_P: Pulsewidth
ω_P: Pump beam waist
I_P: Pump intensity
z_0: Rayleigh range
f_{rep}: Repetition rate
L_R: Resonator length
T_R: Roundtrip time
E_{sat}: Saturation energy
$G^{(2)}$: Second order autocorrelation function
γ: Self amplitude modulation (SAM)
L_P: Separation between two prisms
η: Slope efficiency
g_0: Small signal gain
c: Speed of light
τ_2: Spontaneous lifetime
L_S: Substrate length
g_{th}: Threshold gain

I_L: Laser intensity

L: Loss

B: Magnetic field amplitude

α_L: Material loss

n_2: Nonlinear refractive index

N: Number of longitudinal modes

Z: Optical path

m: Order of diffraction

P_{th}: Threshold power

T: Transmission

λ: Wavelength

k: Wave number

Chapter 1: Introduction

1.1 Historical Review of Mid-IR Lasers

The mid-infrared region of the electromagnetic spectrum covers the wavelength domain roughly from 2 to 5 microns. As a matter of fact, it may depend on the application of interest. In some fields, sometimes people regard larger or narrower regions as mid-infrared. In the literature, semiconductor diode lasers, solid-state lasers and gas lasers were developed in this region. In the case of solid-state lasers, the first mid-infrared laser was developed in 1960. It was a pulsed uranium doped calcium fluoride laser (U^{3+}:CaF_2) operating at 2.6 μm [1]. Two years later, the first continuous-wave operation was obtained with a Dy^{2+}:CaF_2 laser [2]. Both lasers were pumped with a xenon flash lamp source, and they were cryogenically cooled below the room temperature (Typically below 50-70K).

The early mid-infrared lasers had narrow emission bandwidths because incorporated active ions belonged to the rare earth family of the periodic table, such as the ones mentioned above (uranium and dysprosium). After 1963, a new class of mid-IR laser materials emerged, following the invention of transition metal doped fluorides. The first flashlamp pumped tunable mid-IR lasers were, Ni^{2+}:MgF_2, Co^{2+}:MgF_2 and Co^{2+}:ZnF_2 [3, 4]. These mid-infrared lasers had two major difficulties. First, the gain crystals had low emission cross-sections which required cryogenic cooling. Second, the flashlamp pumping

allowed non-radiative transitions and caused overheating of the gain crystal. In 1978, Moulton and co-workers realized that laser pumping would highly reduce the overheating of the gain medium [5]. As a result, they reported the first laser pumped cw operating Ni^{2+}:MgF_2 laser by pumping it with a Nd:YAG laser. The laser was able to operate at 200 K which was a significant improvement in the CW operation of tunable lasers in 1978.

In 1980s and 1990s, the most popular mid-infrared tunable laser was cryogenically cooled Co^{2+}:MgF_2, which is tunable from 1.5 to 2.3 μm. DeLoach and co-workers realized that tetrahedral ZnSe crystal structure provides higher transition probabilities than the octahedral fluorides due to the forbidden 3d-3d transition. They did several spectroscopic experiments on ZnS, ZnSe and ZnTe hosts and doped them with Cr, Co, Ni and Fe transition metal ions. Based on their results, Cr doped zinc chalcogenides showed the best spectroscopic results at room temperature operation [6, 7]. In subsequent years cadmium chalcogenides [8, 9], cadmium telluride [10], and several other combinations were tried as well. Nevertheless, in the case of room temperature operation, Cr:ZnSe remained as the most favorable mid-IR laser material [6]. (For more detailed discussion on spectroscopic properties see Section 1.2.2)

1.2 Review of Earlier Work on Cr:ZnSe Laser

In this section, some of the important milestones in the development of Cr:ZnSe lasers will be summarized. In first section, earlier mode-locked Cr:ZnSe lasers will be described and key results will be underlined. In the second section, spectroscopic properties of the Cr:ZnSe crystal will be introduced. Synthesis methods, energy level diagram, and some structural properties will be discussed.

As we mentioned above the first Cr:ZnSe laser was demonstrated in 1996 by De Loach et al. The laser operated in the gain switched regime, and was pumped with a 10 Hz Co:MgF_2 laser. They further tuned the output of the laser from 2.15 to 2.8 μm [6, 7]. Three years later, Wagner et al reported the first continuous-wave operation [11]. The laser was

pumped with a Tm:YALO laser operating at 1.94 μm, and it delivered as high as 250 mW of output power with a 7% output coupler. Also they tuned it with a Brewster cut prism from 2.14 to 2.76 μm. In the following years, pulsed [12] and cw tuning [13] were demonstrated as well. Demirbas et al reported the broadest tuning in 2006 from 1.88 to 3.1 μm when the Cr:ZnSe laser was intracavity pumped with an optical parametric oscillator (OPO) [12]. The tunability range of some known lasers is summarized in Fig. 1.2.1. As it can be seen, the broadest wavelength range was obtained with the Cr:ZnSe laser.

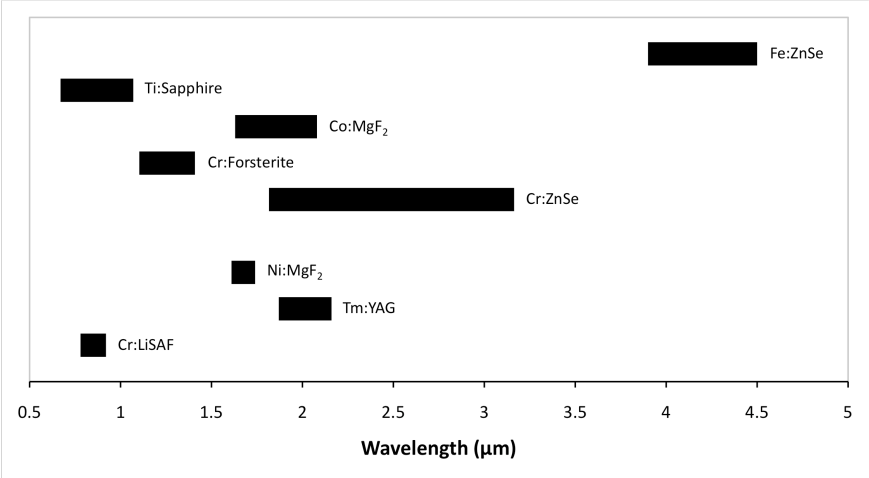

Figure 1.2.1: Spectral tunability range of some important tunable solid-state lasers.

1.2.1 Mode-locked Operation of Cr:ZnSe Laser

Four years after the first demonstration of lasing in Cr:ZnSe [11], the first mode-locked operation was reported in 2000 by Carrig et al [14]. They used an acousto-optic modulator to initiate 4.4-ps pulses with an intracavity power of 2.73-W. In the following year, Sorokina et al reported shorter pulse duration of 4-ps with the same mode locking technique [15]. However, they claimed that the theory of active mode locking does not predict pulses as short as 4-ps. In this case, they proposed that additional pulse shortening occurred as a result of passive mode locking mechanisms. In 2005, the first passively mode

locked Cr:ZnSe laser was demonstrated by using a SESAM (Semiconductor saturable absorber mirror). It delivered 11-ps pulses with output power of 400 mW [16].

On the other hand, theoretical simulations showed that even shorter pulses can be generated with an intensity dependent element and precise dispersion compensation [17]. The first dispersion compensated, SESAM (Semiconductor saturable absorber mirror) mode-locked Cr:ZnSe laser produced pulses below 100-fs [18]. For dispersion compensation, a 5-mm-long sapphire plate was added to the high reflector arm. After a year, the same group had demonstrated even shorter pulses of 80-fs duration using by chirped mirror dispersion compensation. In Section 2.4, a detailed outline of passive mode locking theory will be presented.

1.2.2 Spectroscopic Properties of Cr:ZnSe

In this thesis work, a divalent chromium doped zinc selenide crystal (Cr^{2+}:ZnSe) was used in order to provide the 4-level gain medium. The crystal has the highest emission cross-section compared to the counterparts ($90x10^{-20}cm^2$) [6], and the thermal conductivity of the ZnSe (18W/m.°C) is almost as good as in sapphire (27W/m.°C) [13]. Another favorable spectroscopic property is that, Cr:ZnSe has low excited-state absorption (ESA) cross-section [19]. Hence, very efficient laser operation can be obtained. One drawback is that the thermal lensing of the medium is high since dn/dT for ZnSe is $70x10^{-6}$/K.

Another key benefit of the Cr:ZnSe is that it can be prepared by a cost efficient method called diffusion doping [20, 21]. In this method, the dopant ions (CrSe or Cr powder) and the substrate (ZnSe) are put into an ampoule (See Fig. 1.2.1), and sealed under vacuum. The prepared ampoule is placed inside a furnace at very high temperatures, so that the dopant ions diffuse into the substrate. Since lasers are very sensitive to losses coming from the laser materials, the purity of the final product is very crucial. Therefore, very pure, commercially available ZnSe substrates were selected. Also, in order to lower the unwanted metal oxide contamination even further, the substrate and the dopant were

intentionally put into separate compartments because this allows the diffusion of Cr ions into the ZnSe occur during gas phase.

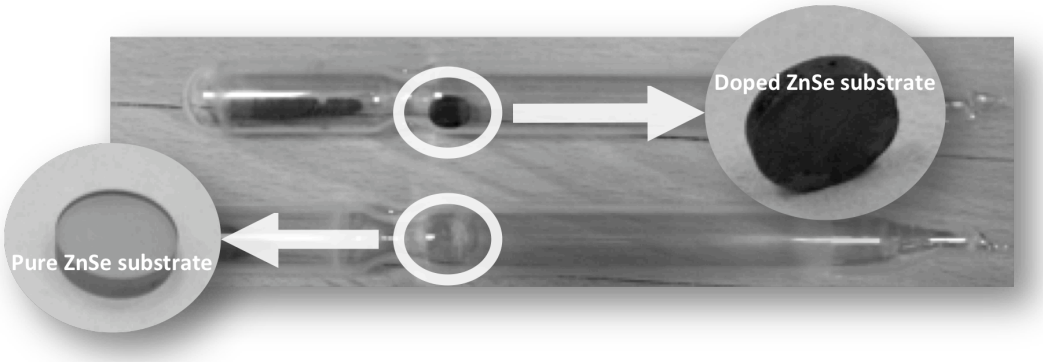

Figure 1.2.2: The image of a diffusion doped and pure ZnSe substrate.

For a typical synthesis, it was put into the furnace above 1000 °C for 1 or 2 days depending on the desired amount of Cr concentration inside the ZnSe. The reader may find more comprehensive discussion of the experimental procedure and spectroscopic analysis that had been made by our group in Ref: [22].

After the diffusion process, Cr^{2+} ions with radius of 0.91Å replace the Zn^{2+} ions of the host with radius of 0.88Å. Since ZnSe crystallize in wurtzite and sphalerite type of structures [23], chromium atoms will be tetrahedrally coordinated by the selenium ions. While fluoride hosts, which are octahedral structures, provide centrosymmetric environment to the dopant ions, ZnSe provides non-centrosymmetric environment to the Cr ions. It gives smaller crystal field splitting [24], and allows infrared emission from the material. The energy levels are predicted by the crystal field theory (See Fig. 1.2.3).

Free ion energy of ^5D splits into excited state of ^5E and ground state of $^5T_2$ due to the effect of the crystal field. They further split by the Jahn-Teller effect because an unstable non-linear molecular system will distort itself until reaching the lowest symmetry and the lowest energy to be able to remove degeneracy from the system [25].

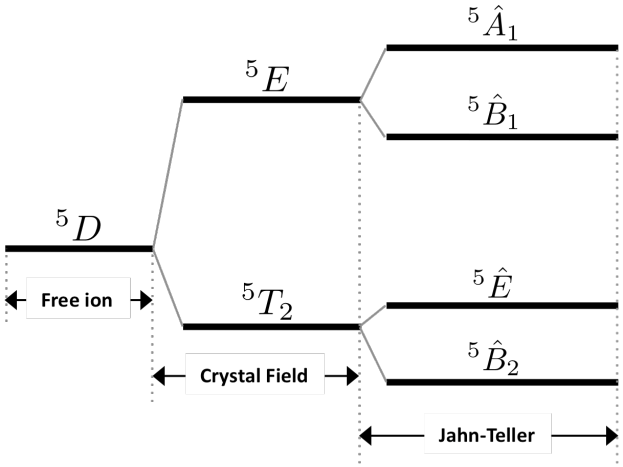

Figure 1.2.3: The energy level diagram of Cr:ZnSe crystal, they were predicted by the crystal field theory [26].

The absorption spectrum of pure and doped Cr:ZnSe crystal is seen in Fig. 1.2.4. There are two significant contributions originating from the existence of Cr ions. One is the absorption band centered around 1.8 μm due to $^5T_2 \rightarrow {}^5E$ transition. Other contribution is the shift of short wavelength absorption edge to longer wavelengths due to existence of Cr^{+1} ions inside the crystal. The short wavelength shift provides an indirect measure of the Cr concentration because Cr^{1+} concentration increases with the addition of more ions into the crystal.

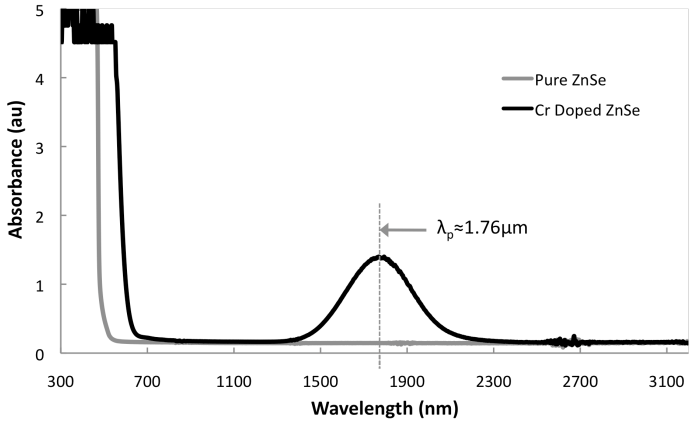

Figure 1.2.4:Absorption spectrum of the pure and Cr doped ZnSe crystal.

The typical emission spectrum of a Cr:ZnSe sample can be seen in Fig. 1.2.5 [27]. The sample was excited with a Cr:YAG laser source operating at 1.49 μm. The emission spectrum was measured with a Czerny-Tuner type monochromator, and it was recorded with a PbS detector. The emission spectrum has a peak around 2 μm with 600nm of width.

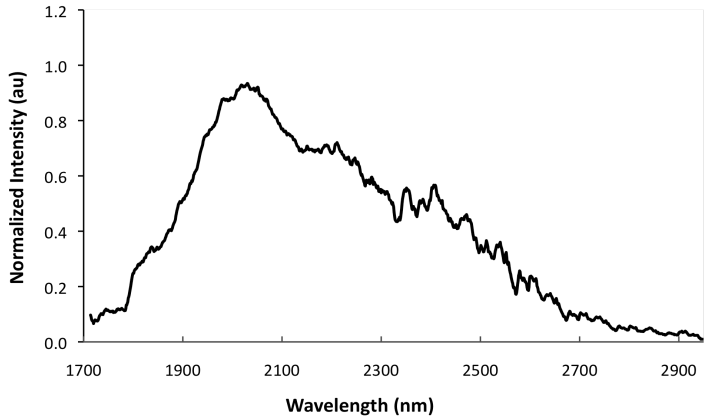

Figure 1.2.5: Typical emission spectrum of the Cr:ZnSe crystal.

In addition, for the fluorescence lifetime measurement, the sample was pumped with a 1kHz pulsed OPO laser operating at 1.57 μm. From the Figure, the lifetime of the ions was determined as 4.5 μs, by doing a single exponential fit to the experimental data shown in Fig. 1.2.6 [27].

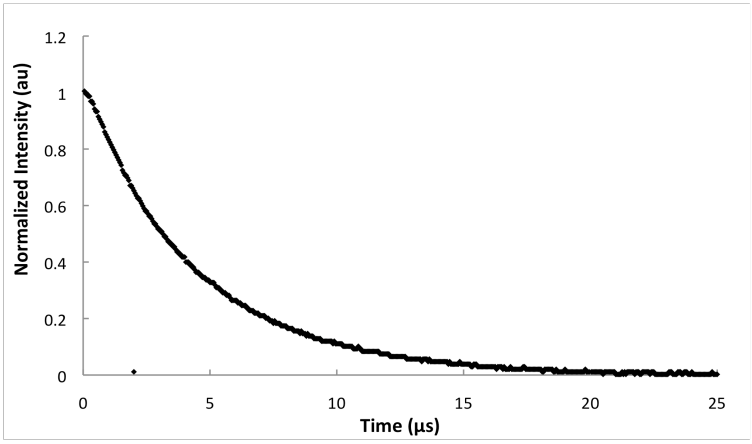

Figure 1.2.6: Time dependent fluorescence decay of Cr:ZnSe.

1.3 Applications of Ultrashort Pulses in the Mid-Infrared

One of the recent applications for the development of femtosecond mid-infrared lasers is high harmonic generation (HHG). In this method, intense pulses are used to obtain coherent radiation in the deep UV or soft x-ray region. Based on the numerical calculations done by Gordon and Kaertner [28], when the wavelength of intense driving field increases beyond 1.5 μm, the spectral cutoff energy of generated harmonics increases as well (See Fig. 1.3.1). Another important requirement to generate high harmonics is that the pulse energy of the femtosecond laser should be on the order of micro- or mili-joules. However, typical femtosecond lasers only produce nano-joules of pulse energies which is not sufficient. As a result, pulse energies need to be amplified with a technique called chirped pulse amplification (CPA).

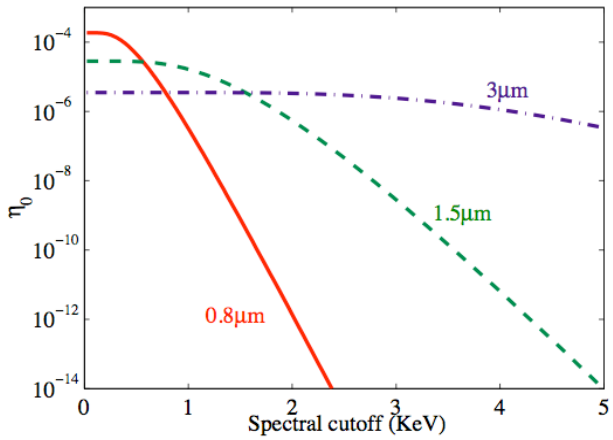

Figure 1.3.1: Spectral cutoff energy and efficiency variation with respect to center wavelength of the driving field.

The chirped pulse amplifier includes three components. The first one is the stretcher, which stretches femtosecond pulses to picoseconds. The second one is the amplifier, where stretched pulses are amplified inside a gain switched laser. Finally, amplified pulses are compressed with a compressor to initial pulse durations. One group in 1999 employed a

CPA with a Cr:Forsterite laser and they successfully amplified 43 kW peak power up to approximately 1.5 GWs [29].

There are numerous other applications that can use femtosecond mid-infrared lasers, such as metrology [30, 31], spectroscopy [32, 33], and nonlinear optical conversion [34, 35].

Chapter 2: Theoretical Background

2.1 Gaussian Beams

At long distances away from a point source, electromagnetic waves have nearly planar wavefronts. On the other hand, when dealing with laser beams which are confined in the plane that is perpendicular to the direction of propagation, such assumption is no longer valid. In this case, solutions of Maxwell's equations show that the fields with Gaussian transverse distribution can satisfy boundary conditions on spherical surfaces and have transverse confinement. They are referred to as Gaussian beams.

When the wavelength of the beam is much smaller than the initial spotsize, Gaussian beams are nearly transverse electromagnetic (TEM) waves. This means that the electric and magnetic field vectors are perpendicular to the direction of propagation as it can be seen from Fig. 2.1.1. In the figure, $\vec{S}$ represents the pointing vector, which is the energy flux of the electromagnetic field. For linear mediums it is parallel with the direction of propagation.

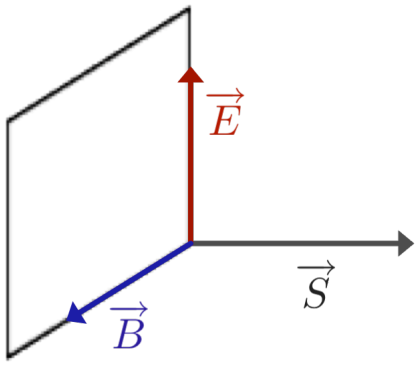

Figure 2.1.1: Orientation of the electric and magnetic fields for a TEM wave.

In the paraxial regime, the amplitude distribution of the electric field in the transverse plane is

$$\psi_0 = exp\left[-j\left[P(z) + \frac{kr^2}{2q(z)}\right]\right]. \qquad 2.1.1$$

Above, *P(z)* describes the axial phase factors and *q(z)* is known as the Gaussian q-parameter. The q-parameter provides information about the radius of curvature *R(z)* and spotsize *ω(z)* and it is given in terms of *R(z)* and *ω(z)* by

$$\frac{1}{q(z)} = \frac{1}{R(z)} - j\frac{\lambda_0}{\pi n\omega^2(z)}. \qquad 2.1.2$$

The function *R(z)* gives the radius of the equiphase surface of the beam as a function of position and can be calculated from

$$R(z) = z\left[1 + \left(\frac{z_0}{z}^2\right)\right]. \qquad 2.1.3$$

The spotsize function *ω(z)* is given by

$$\omega(z)^2 = \omega_0^2\left[1 + \left(\frac{z}{z_0}\right)^2\right], \qquad 2.1.4$$

which characterizes the transverse confinement of the Gaussian beam. In other words, it gives the radial position where the field decreases to 1/e of its maximum value.

In the above equations, z_0 is the distance between the location of the beam waist and the position where the spotsize becomes $\sqrt{2}\,\omega_0$. This is also referred to as the Rayleigh range and is given in terms of wavelength (λ) and beamwaist (ω_0) as

$$z_0 = \frac{\pi\omega_0^2}{\lambda} \qquad 2.1.5$$

in vacuum. Fig. 2.1.2 shows the spotsize variation of a Gaussian beam and the Rayleigh range.

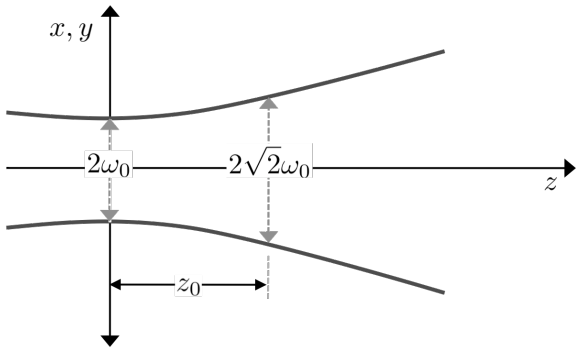

Figure 2.1.2: Sketch of a Gaussian beam, showing the Rayleigh range and the beam waist.

The above discussion is valid for a diffraction limited Gaussian beam. However, in reality, most of the laser beams deviate from the ideal case. For a non-ideal Gaussian beam, a parameter known as the M-square (M^2) factor is used to show the deviation of a Gaussian beam from ideal diffraction limited propagation. For a non-ideal Gaussian beam, the Rayleigh range becomes

$$z_0 = \frac{\pi\omega_0^2}{M^2\lambda}. \qquad 2.1.6$$

Therefore, as can be seen from Eq. 2.1.6 when M^2 equals 1, the beam is diffraction limited. When $M^2>1$, Rayleigh range is smaller than the ideal case, meaning that the beam expands with a larger divergence angle.

2.2 ABCD Analysis of the Resonator

2.2.1 Ray Optics

The behavior of light can be predicted after passing through a thin lens, or a material interface by using well-established relations. However, in the case of an optical system, which includes many optical elements (See Fig. 2.2.1), a systematic method called ray transfer matrix is used to simplify the calculations. In this method, light is assumed to be a paraxial ray (i.e. $sin\theta \sim \theta$) and a 2x1 matrix describes it as

$$\overrightarrow{U} = \begin{bmatrix} r \\ \theta \end{bmatrix}, \qquad 2.2.1$$

where r is the ray height and θ is the angle of inclination.

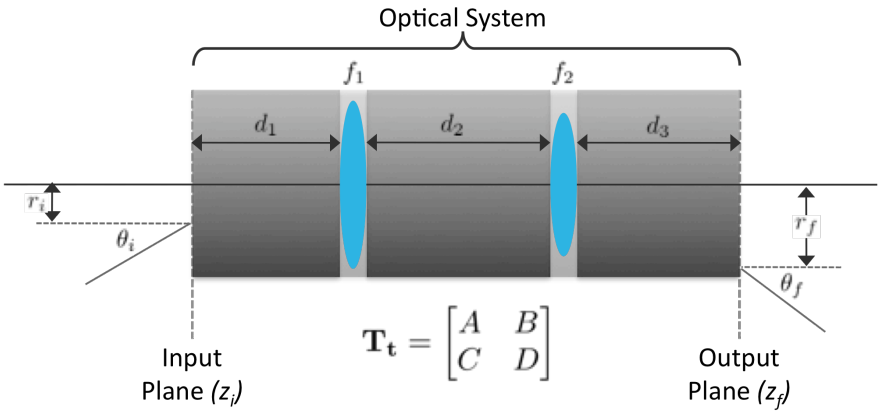

Figure 2.2.1: An example optical system for ABCD analysis.

In order to be clear on how to adapt ray tracing method to an optical system, consider the one that is illustrated in Fig. 2.2.1. In this optical system, two lenses and three free-space displacements exist. The free space regions with separations of d_1, d_2 and d_3 are indicated with dark color shade, where light color shaded ones indicate the thin lenses with focal lengths of f_1 and f_2. As a result, the equivalent ray transfer matrix of this optical system is

$$\mathbf{T_t} = \mathbf{T_{d3}}\mathbf{T_{f2}}\mathbf{T_{d2}}\mathbf{T_{f1}}\mathbf{T_{d1}}. \quad 2.2.2$$

It is the matrix multiplication of corresponding transfer matrices beginning from the output plane, z_f, and continues until reaching the input plane, z_i. Each optical component has a unique transfer matrix. For common optical elements such as thin lens, material interface and a curved mirror, the ray transfer matrices are well known and listed in Table 2.2.1. For the specific example illustrated in the Figure 2.2.1, the thin lens and the free space matrices are multiplied in Eq. 2.2.2.

Component	Ray transfer matrix
Free space	$T = \begin{bmatrix} 1 & d \\ 0 & 1 \end{bmatrix}$
Thin lens	$T = \begin{bmatrix} 1 & 0 \\ -\frac{1}{f} & 1 \end{bmatrix}$
Concave mirror	$T = \begin{bmatrix} 1 & 0 \\ -\frac{2}{R} & 1 \end{bmatrix}$
Material Interface	$T = \begin{bmatrix} 1 & 0 \\ 0 & \frac{n_1}{n_2} \end{bmatrix}$

Table 2.2.1: Summary of some common ray transfer matrices.

The height and the angle of inclination at output plane with respect to input plane is

$$\begin{bmatrix} r_f \\ \theta_f \end{bmatrix} = \mathbf{T_t} \begin{bmatrix} r_i \\ \theta_i \end{bmatrix}. \quad 2.2.3$$

It is linked with the equivalent ray transfer matrix ($\mathbf{T_t}$) of the optical system in Fig. 2.2.1 which is

$$\mathbf{T_t} = \begin{bmatrix} 1 & d_3 \\ 0 & 1 \end{bmatrix} \begin{bmatrix} 1 & 0 \\ -\frac{1}{f_2} & 1 \end{bmatrix} \begin{bmatrix} 1 & d_2 \\ 0 & 1 \end{bmatrix} \begin{bmatrix} 1 & 0 \\ -\frac{1}{f_1} & 1 \end{bmatrix} \begin{bmatrix} 1 & d_1 \\ 0 & 1 \end{bmatrix}. \quad 2.2.4$$

2.2.2 Gaussian Beams

ABCD law can be used to predict the behavior of Gaussian beams as well. For Gaussian beams, the complex beam parameters at the input and output plane are related by

$$\frac{1}{q_f} = \frac{C + D(1/q_i)}{A + B(1/q_i)}. \qquad 2.2.5$$

Above, q_i and q_f are complex beam parameters of input and output plane, respectively. Here the ABCD parameters belong to the equivalent transfer matrix of the optical system.

As an example, the beamwaist of a frequently used laser resonator will be determined. During our experiments, an x-fold resonator design was used as seen in Fig. 2.2.2. Since the laser beam travels back and forth in the resonator, it enables us to use the same plane, say M4, as the input and the output plane of the optical system.

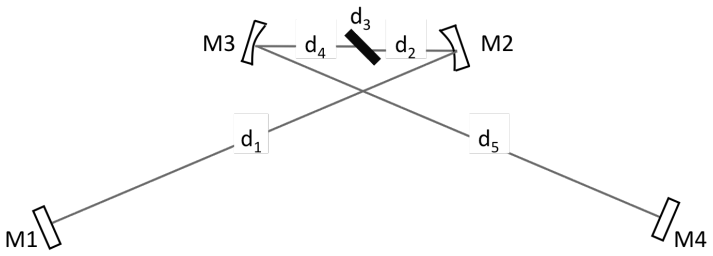

Figure 2.2.2: Typical x-fold resonator design used during our experiments.

ABCD equivalent of the resonator is seen in Fig. 2.2.3. Here, curved mirrors are regarded as thin lenses.

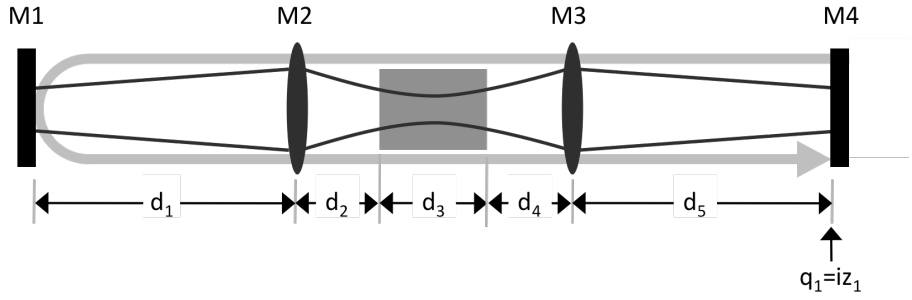

Figure 2.2.3: ABCD equivalent of an x-cavity resonator shown in Fig. 2.2.2.

By following the direction of the arrow in Fig. 2.2.3, the equivalent ray transfer matrix of this resonator can be calculated from

$$T = \begin{bmatrix}1 & d_1\\ 0 & 1\end{bmatrix}\begin{bmatrix}1 & 0\\ -1/f & 1\end{bmatrix}\begin{bmatrix}1 & d_2\\ 0 & 1\end{bmatrix}\begin{bmatrix}1 & 0\\ 0 & 1/n\end{bmatrix}\begin{bmatrix}1 & d_3\\ 0 & 1\end{bmatrix}\begin{bmatrix}1 & 0\\ 0 & n\end{bmatrix}\begin{bmatrix}1 & d_4\\ 0 & 1\end{bmatrix}$$
$$\begin{bmatrix}1 & 0\\ -1/f & 1\end{bmatrix}\begin{bmatrix}1 & d_5\\ 0 & 1\end{bmatrix}\begin{bmatrix}1 & d_5\\ 0 & 1\end{bmatrix}\begin{bmatrix}1 & 0\\ -1/f & 1\end{bmatrix}\begin{bmatrix}1 & d_4\\ 0 & 1\end{bmatrix}\begin{bmatrix}1 & 0\\ 0 & n\end{bmatrix}\begin{bmatrix}1 & d_3\\ 0 & 1\end{bmatrix} \qquad 2.2.6$$
$$\begin{bmatrix}1 & 0\\ 0 & 1/n\end{bmatrix}\begin{bmatrix}1 & d_2\\ 0 & 1\end{bmatrix}\begin{bmatrix}1 & 0\\ -1/f & 1\end{bmatrix}\begin{bmatrix}1 & d_1\\ 0 & 1\end{bmatrix} = \begin{bmatrix}A & B\\ C & D\end{bmatrix}.$$

Here *n* is the refractive index of the gain medium and *f* is the focal length of the curved mirrors (f=R/2). Since the same input and output plane on the mirror M4 is used, Eq. 2.2.5 will become a quadratic equation in the form of

$$\frac{1}{q_1} = \frac{C + D(1/q_1)}{A + B(1/q_1)}. \qquad 2.2.7$$

To be able to comment on the solution of the above equation, one thing should be kept in mind. The M4 mirror creates a flat boundary condition, so the real part of q parameter (q_1) is zero and it becomes a purely imaginary number. Since the imaginary part of the q parameter is defined as the Rayleigh range (See Eq. 2.1.2), we end up with the result

$$\mathrm{Im}(q_1) = z_1 = \frac{|B|}{\sqrt{1 - \left(\frac{A+D}{2}\right)^2}}. \qquad 2.2.8$$

Now the Rayleigh range (z_1) as well as the complex parameter (q_1) of the spot on M4 mirror are known. Hence, the input q parameter at the edge of the crystal (q_3) can be calculated (See Fig. 2.2.4-a). Required transfer matrix is

$$T' = \begin{bmatrix}1 & d_4\\ 0 & 1\end{bmatrix}\begin{bmatrix}1 & 0\\ -1/f & 1\end{bmatrix}\begin{bmatrix}1 & d_5\\ 0 & 1\end{bmatrix} = \begin{bmatrix}A' & B'\\ C' & D'\end{bmatrix}. \qquad 2.2.9$$

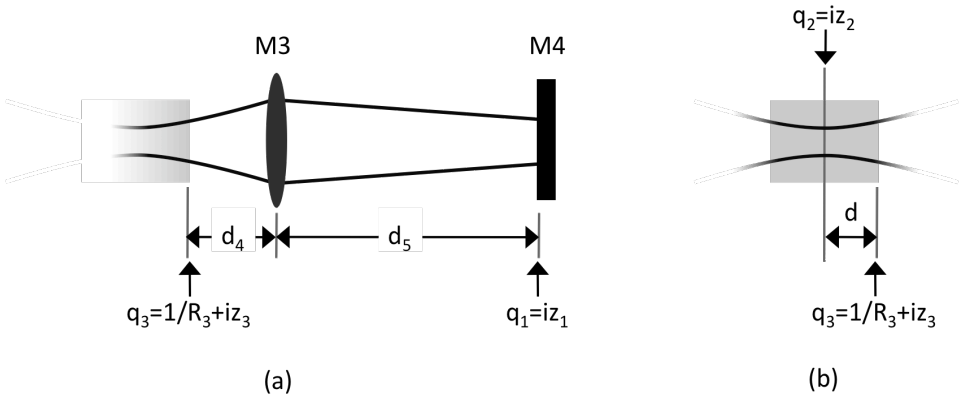

Figure 2.2.4: (a) Part of the equivalent resonator which enables the determination of q_3. (b) Part of the equivalent resonator which enables the determination of q_2 and beamwaist location inside the crystal.

When the beam propagates inside the crystal (See Fig. 2.2.4-b), the distance of the beamwaist (d), and the corresponding values of the Rayleigh range (z_2) and the beamwaist (ω_{02}) are derived as

$$d = -\frac{n(B'D' + A'C'z_1^2)}{D'^2 + C'^2 z_1^2}, \qquad 2.2.10$$

$$z_2 = \frac{nz_1}{D'^2 + C'^2 z_1^2}, \qquad 2.2.11$$

and

$$\omega_{02} = \sqrt{\frac{z_2 \lambda}{n\pi}}, \qquad 2.2.12$$

respectively.

Finally, when the beamwaist was calculated based on input parameters listed in Table 2.2.2, it was 32.8 μm at the center of the stability region.

d_1 (cm)	d_2 (cm)	d_3 (cm)	d_4 (cm)	d_5 (cm)	f (cm)	n
65.5	5.62	2.6	5.62	83	5	2.44

Table 2.2.2: Experimental parameters that were used in our experiments.

Moreover, calculated variation of the beamwaist and the distance can be seen in Fig. 2.2.5 and 2.2.6, respectively. Throughout the calculations, spotsize and the distance are assumed to be zero when the cavity is not stable i.e. when we cannot find a self-consistent solution of Eq. 2.2.7.

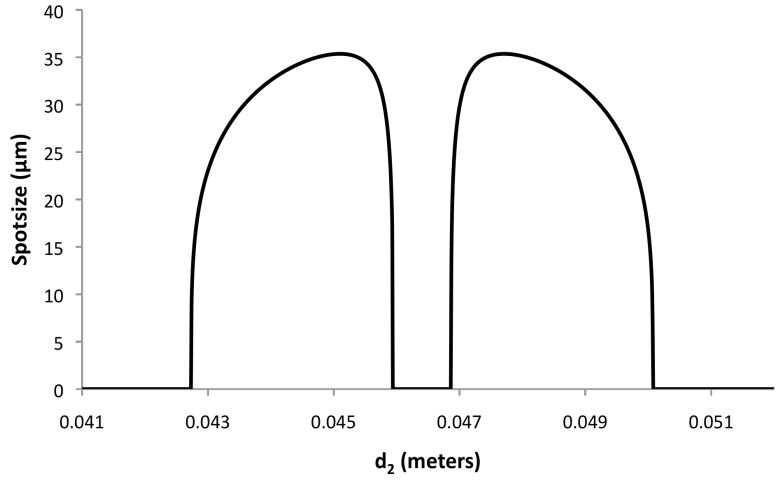

Figure 2.2.5: Calculated variation of the beamwaist inside the gain crystal as a function of the distance between the edge of the crystal and the first mirror.

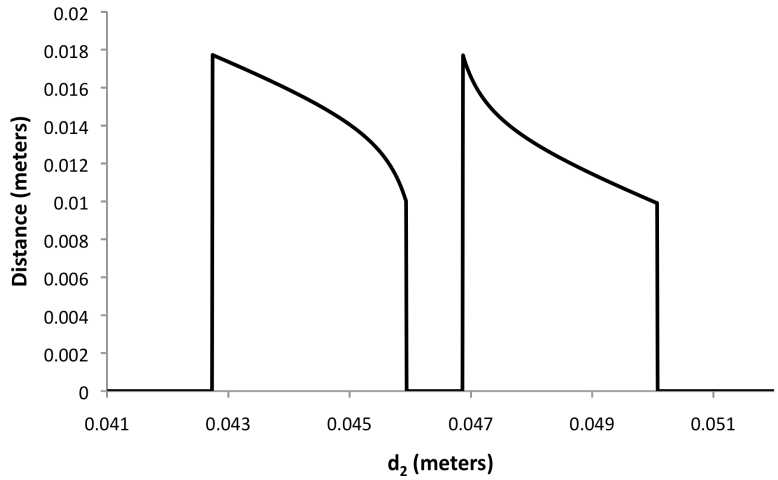

Figure 2.2.6: Variation of the beam waist position inside the crystal with respect to the distance between the edge of the crystal and the first mirror.

2.3 Laser Fundamentals

In this section, some of the important laser concepts will be summarized. In the first section, four level gain mechanism and the emission types are described. In the second section, optical gain from the laser materials is modeled and threshold power, gain, and loss are calculated from the rate equations. In the last section, power efficiency curves and loss analysis are described.

2.3.1 Gain Mechanism

The gain medium in which optical amplification takes place, is the most crucial element of a laser. In the case of solid-state laser materials, they contain optically active ions which are incorporated in transparent host materials. These active ions (usually rare earth (RE) or transition metal (TM) ions) are responsible for the emission characteristics of the solid-state laser materials. In our experiments, transition metal chromium ions were incorporated into the zinc selenide (ZnSe) polycrystalline host. It has a maximum absorption band centered around 1.8 μm and a broad emission between 1.9-3.0 μm.

Currently available lasers can be classified into many groups depending on their gain mechanisms. However, in this thesis work, only four-level gain systems will be emphasized. In four level systems, the lowest energy level is regarded as the ground state and the highest one as the excited state. In addition to those levels, two more energy levels are formed near the excited state and the ground level as seen in Fig. 2.3.1.

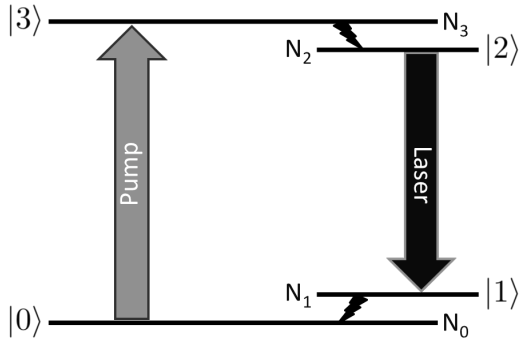

Figure 2.3.1: Energy level diagram of a 4-level laser system.

When an absorbed photon excites the active ion, the ion is promoted from the ground to excited state. Right after the excitation, excited ion rapidly decays to nearby energy level (|2>) without emitting a photon. Depending on the spontaneous emission lifetime of the atom, it stays at level 2 for a while and then relaxes to level 1 by emitting a photon with photon energy equal to the difference between the energies of the two levels. This type of emission is known as spontaneous emission and occurs in random directions. Another type of emission occurs when the decay is stimulated by other photons. This results in the generation of coherent, directional photons and the process is known as stimulated emission.

The four level gain system is an efficient system because the population inversion condition is always met under the presence of a pump source. This means that the ion density of the upper laser level is always greater than that at the lower laser level which is nearly empty due to its fast relaxation time to ground state. Positive population inversion is essential for a laser to operate and it will be covered in the following sections. Population inversion does not necessarily give net amplification. Net gain is achieved when the gain exceeds the losses.

2.3.2 Modeling of Optical Gain

Time rate of change of upper state population density (N_2) equals

$$\frac{dN_2}{dt} = \frac{\sigma_a I_P}{h\nu_P} N_1 - \frac{N_2}{\tau_2} - \frac{\sigma_e I_L}{h\nu_L} N_2. \qquad 2.3.1$$

Here σ_a and σ_e are the absorption and emission cross sections, respectively, I_P is the pump intensity, I_L is the laser intensity, v_p and v_L are the frequency of pump and laser photons. Finally, N_1 is the population density of level 1 in Fig. 2.3.1.

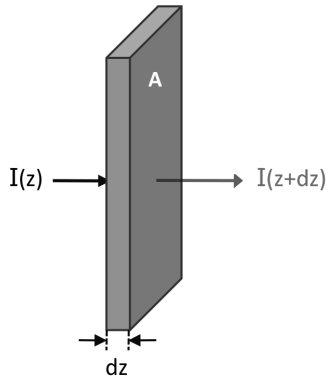

Figure 2.3.2: Hypothetical gain medium with thickness of dz and area of A.

Furthermore, fractional single pass power gain can be obtained by assuming a thin medium of length dz, and cross-sectional area A (See Fig. 2.3.3). The number of photons that contributes to laser emission will be

$$\frac{(I_L(z+dz)-I_L(z))A}{h\nu_L} = (N_2)\left(\frac{\sigma_e I_L}{h\nu_L}\right)(A\mathrm{d}z). \qquad 2.3.2$$

Since intensity is power per unit area, the fractional change in beam power is

$$g = \frac{\Delta P_L}{P_L} = \frac{(I_L(z+dz)-I_L(z))A}{I_L A} = N_2\sigma_e L_C \qquad 2.3.3$$

where the L_C is the length of the gain medium and P_L is the laser power.

It can be shown that g and P_L satisfies the coupled differential equations of

$$\frac{\mathrm{d}g}{\mathrm{d}t} = \frac{g_0}{\tau_2} - \frac{1}{\tau_2}g_0 - \frac{P_L}{E_{sat}}g \qquad 2.3.4$$

and

$$\frac{\mathrm{d}P_L}{\mathrm{d}t} = \frac{2g}{T_R}P_L - \frac{1}{\tau_P}P_L. \qquad 2.3.5$$

Here the roundtrip time (T_R), cavity photon lifetime (τ_C) and the saturation energy (E_{sat}) are given by

$$T_R = \frac{2L_R}{c}, \tag{2.3.6}$$

$$\tau_C = \frac{2L_R/c}{2\alpha_L L_C + \frac{1}{2}\ln\frac{1}{R_1 R_2}}, \tag{2.3.7}$$

and

$$E_{sat} = \frac{h\nu_L}{\sigma_e} A, \tag{2.3.8}$$

respectively.

At laser threshold, the small-signal gain (g_0) is equal to losses. As a result, the threshold gain at steady state becomes

$$g_{th} = \frac{T_R}{2\tau_C}. \tag{2.3.9}$$

When the above definitions of T_R and τ_C are substituted into Eq. 2.3.9, threshold gain will be equal to

$$g_{th} = \alpha_L L_C + \frac{1}{2}\ln\frac{1}{R_1 R_2}. \tag{2.3.10}$$

Threshold gain is proportional to the population inversion $\Delta N=N_2$ and as the pump power P_P increases, the small-signal gain will increase. The corresponding threshold power to attain laser can be obtained for a Gaussian pump and laser beams from [36]

$$P_{th} = \frac{\pi h\nu_P(\omega_L^2 + \omega_P^2)(T + L)}{4\eta_a \tau_2 \sigma_e}. \tag{2.3.11}$$

In the above equation, ω_L and ω_P are laser and pump beam waists, respectively, η_a is the fractional absorbed pump power by the gain medium, T is the total transmission of mirrors, τ_2 is the spontaneous lifetime, and L is total passive loss. It can be easily seen that the threshold pump power depends on numerous parameters, some of them can be adjusted and some of them are fixed for a certain laser system. The minimum spotsizes of laser and

pump beams, minimum amount of passive loss and high pump absorption enables low-threshold operation.

2.3.3 Continuous-wave (CW) Operation

The gain crystal, Cr:ZnSe, operates in continuous-wave at room temperature. Continuous-wave operation means that the output power of a laser is constant as a function of time.

The passive loss of the resonator can be easily estimated from the power efficiency data. In Fig. 2.3.3, a typical power efficiency curve is seen. The threshold power and slope efficiency can be determined from this curve.

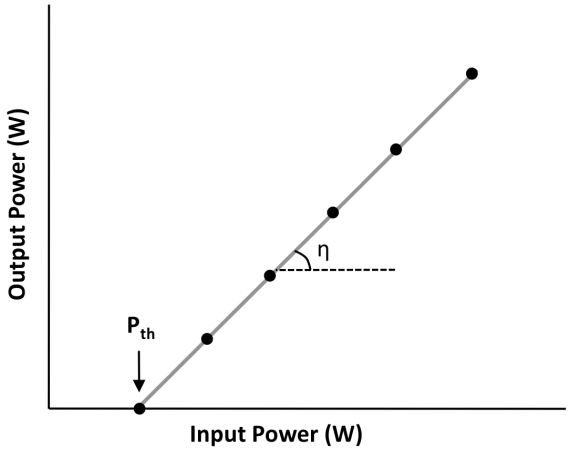

Figure 2.3.3: Typical power efficiency curve, η is the slope efficiency.

After determining the slope efficiency *(η)* from experimental data, the equation

$$\eta = \frac{\lambda_P}{\lambda_L}\frac{T}{T+L}\eta_a \qquad 2.3.12$$

can be used to estimate passive losses of the resonator. Here λ_P and λ_L are wavelength of the pump and the laser beam, respectively. T is the transmission of the output coupler, η_a is the fraction of absorbed pump power in the gain medium and L is the passive loss of the resonator.

If two sets of efficiency curves are taken with different output coupler transmission values, the loss can be determined from

$$\frac{\eta_{T1}}{\eta_{T2}} = \frac{T_2 + L}{T_1 + L}\frac{T_1}{T_2} \qquad 2.3.13$$

where T_1 and T_2 are the transmission values of the output couplers, L is the passive loss of the resonator, and η_{T1} and η_{T2} are the slope efficiencies of the efficiency curves taken with T_1 and T_2, respectively.

2.4 Mode Locking Theory

Femtosecond or picosecond pulses can be generated from a solid-state laser by a method called mode locking. It requires constant phase relation between the longitudinal modes oscillating inside the cavity. In Figure 2.4.1, the relative amplitudes and the phase relations are shown for both types of operations.

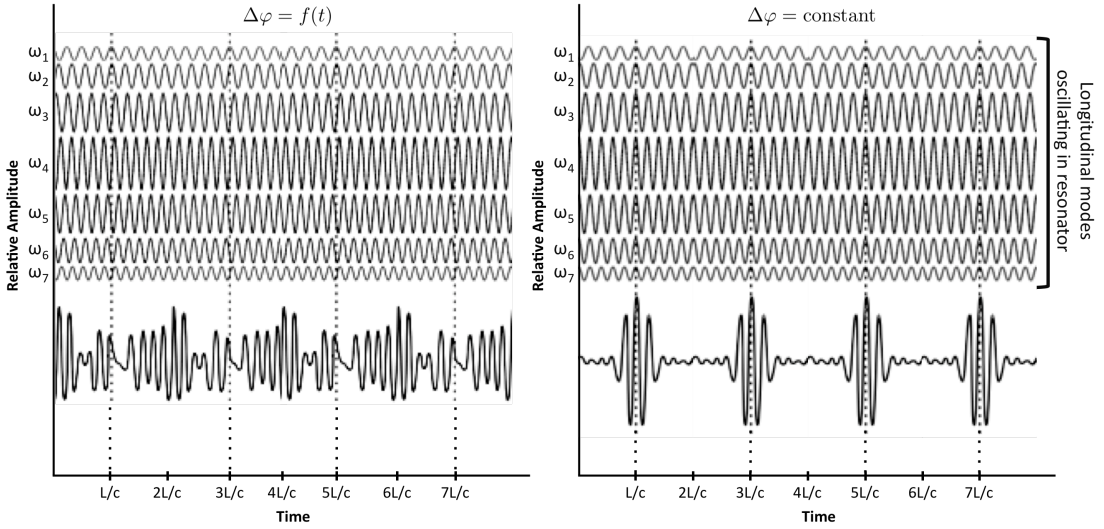

Figure 2.4.1: Time evolution of (a) free running laser and (b) mode-locked laser.

Left hand side plot illustrates a typical free-running laser in which resonant modes are constantly interfering with each other. Hence, they cannot be localized at a particular time interval. In contrast, right hand side plot shows the time dependent behavior of a mode-

locked laser in which modes are oscillating with constant phase relation. Notice that, in the case of mode-locked operation, all the resonant modes have the maximum at the same time. Consequently, they add up constructively and form a wave packet localized at a particular time instant. Resulting wave packets are equally spaced by a temporal separation of $2L_R/c$, and corresponding repetition rate is

$$f_{rep} = \frac{c}{2L_R}. \qquad 2.4.1$$

When the number of longitudinal modes (*N*) oscillating inside the resonator increases, the width of the resulting pulse will be narrower. Since longitudinal modes are limited with the gain bandwidth of the material, broad gain bandwidth is more favorable in the case of ultrashort pulse generation.

Assume that the center frequency of the gain bandwidth is ω_0, and there are ±m additional modes oscillating above and below the center frequency as illustrated in Fig. 2.4.2.

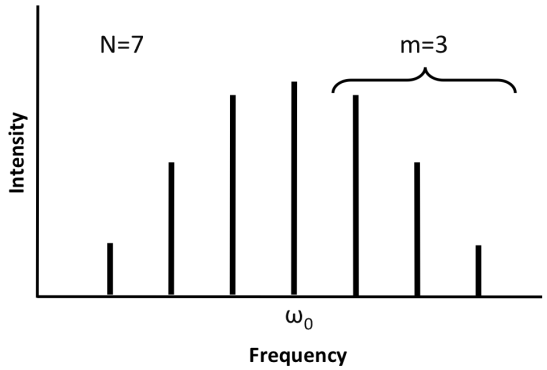

Figure 2.4.2: Representative figure on oscillating resonant modes, where N=7 and m=3.

As a result, the total number of longitudinal modes will be *N=2m+1*. The electric field of arbitrary oscillations can be calculated from

$$E(t) = \sum_{n=-m}^{m} E_n \exp i \left[\left(\omega_0 + n\frac{2\pi}{T_R} \right) t + \varphi_n \right] \qquad 2.4.2$$

where E_n and φ_n are electric field amplitude and phase of the nth mode. Now assume that electric field amplitudes (E_0) of the modes are equal to each other and their phase (φ_0) is equal to zero. Hence, Eq. 2.4.2 becomes

$$E(t) = E_0 \sum_{n=-m}^{m} \exp\left[i\left(\omega_0 + n\frac{2\pi}{T_R}\right)t\right], \qquad 2.4.3$$

where T_R is the roundtrip time and equals $2L_R/c$. When the summation is done, resulting electric field has the form

$$E(t) = E_0 \left[\frac{1 - \exp iN(2\pi/T_R)t}{1 - \exp i(2\pi/T_R)t}\right] \exp i\omega_0 t. \qquad 2.4.4$$

When the electric field is converted to intensity, it is proportional to the following relation for a mode-locked laser:

$$I(t) = E(t)E^*(t) = E_0^2 \frac{\sin^2(N\pi t/T_R)}{\sin^2(\pi t/T_R)}. \qquad 2.4.5$$

Remember that the electric field amplitudes of the modes were assumed to be constant. However, in reality, the amplitudes vary as a function of frequency. In the case of passively mode-locked lasers, generated pulse profile follows the hyperbolic secant distribution in the time domain in the form

$$I(t) = I_0 \mathrm{sech}^2(t/\tau). \qquad 2.4.6$$

The reason why it is hyperbolic secant will be the subject of the next section. For a transform limited sech^2 type pulse, the time bandwidth product is further given by

$$\tau_p \Delta\nu = 0.315. \qquad 2.4.7$$

Even though there are lots of different methods available to force a constant phase relation between longitudinal modes, they can be classified into two main categories namely active and passive mode locking. In the case of active mode locking, there is a fast

acousto-optical switch that is used to initiate ultrashort pulses. However, for passive mode locking, an intensity dependent nonlinearity enables the selection of the high-intensity spikes instead of low-intensity signals of the circulating beam. As a result, intense fluctuations see lower loss and higher gain. One more requirement is that, modulation duration of the active or passive element should be near the duration of the fluctuation itself. When the generated pulse durations are compared for both methods, the passively mode-locked lasers are able to produce the shortest possible pulses. This thesis work mainly focuses on Kerr lens mode locking which is an example of passive mode locking.

2.4.1 Kerr Lens Mode Locking (KLM)

In this technique, a nonlinear material property called Kerr effect is used to produce ultrashort pulses. At this point, the Kerr effect should be mentioned shortly, which is the intensity-dependent response of the material to light. At high intensities, the refractive index of the material becomes a function of intensity as

$$n = n_0 + n_2 I. \tag{2.4.8}$$

Here n_0 is the contribution to refractive index at low intensities and n_2 is known as the nonlinear index coefficient. Since the laser beam is assumed to have a Gaussian beam profile, which means that the center of the beam is more intense compared to the edges (See Fig. 2.4.3), it will be focused due to the Kerr effect.

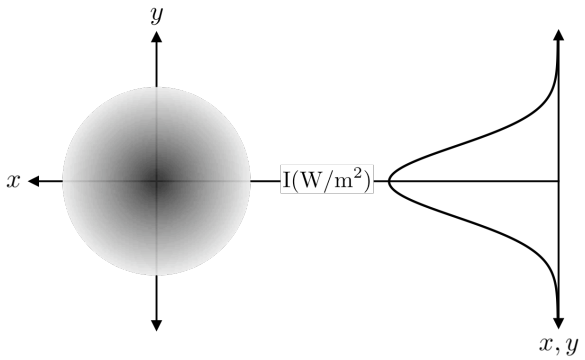

Figure 2.4.3: Transverse intensity distribution of a laser beam.

Notice that it scales with the value of the nonlinear refractive index (n_2), so that high n_2 requires less intense light for self-focusing of the beam. In this respect, Fig. 2.4.4 explains how Kerr effect is used to initiate ultrashort pulses. The figure shows the gain medium, the pump beam and the laser beam profiles. When the positions of the curved mirrors are carefully adjusted, high intensity region of the beam undergoes focusing (in Figure it is represented with the dashed line) and overlaps better with the pump. In order to obtain KLM, pump beam must occupy a smaller volume than the laser beam. Therefore, intense beam experiences higher optical gain and this favors the oscillation of the laser in the mode-locked regime.

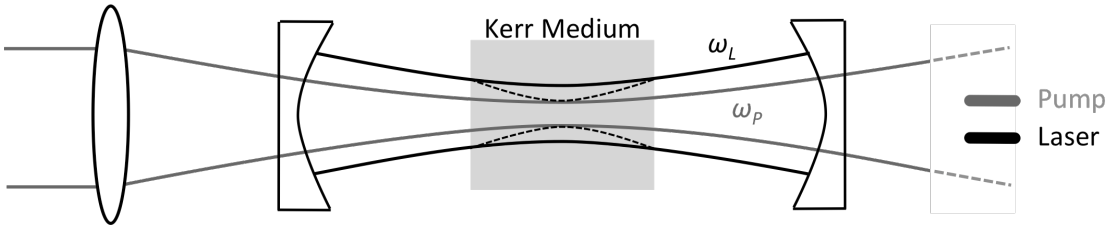

Figure 2.4.4: Schematic of a basic resonator to describe how Kerr lensing is employed to produce ultrashort pulses.

In Ref: [17] Kerr effect is modeled as a fast saturable absorber. The master equation for the field amplitude "a" can be written as

$$\frac{1}{T_R}\frac{\partial}{\partial T}a = (g-l)a + \left(\frac{1}{\Omega_f^2} + jD\right)\frac{\partial^2}{\partial t^2}a + (\gamma - j\delta)|a|^2 a. \qquad 2.4.9$$

Here $|a|^2$ corresponds to the instantaneous power. T_R is the cavity roundtrip time, g and l are the gain and loss, respectively, Ω_f is the gain bandwidth, γ is the self amplitude modulation (SAM) coefficient, δ is the Kerr coefficient, and D is the group velocity dispersion parameter. Finally, t represents small time scale of the order of pulsewidth, and T represents large time scales comparable to cavity roundtrip times. In addition Kerr coefficient (δ) is given by

$$\delta = \frac{2\pi n_2 L_C}{\lambda_0 A_{eff}}. \qquad 2.4.10$$

Here n_2 is the nonlinear refractive index (m^2/W), L_C is the crystal length, λ_0 is the central wavelength, and A_{eff} is the effective area of the beam. Steady state (d/dT=0) solution of the differential equation in Eq. 2.4.9 is [17, 37]

$$a(t) = A_0 \mathrm{sech}^{1+j\beta}\left(\frac{t}{\tau}\right). \qquad 2.4.11$$

Here β is the chirp parameter and due to the large gain bandwidth of the laser, it is assumed to be zero.

For small SAM coefficient ($\gamma \approx 0$), weak filtering due to broad gain bandwidth, Eq. 2.4.9 simplifies to

$$\frac{1}{T_R}\frac{\partial}{\partial T}a = -jD\frac{\partial^2}{\partial t^2}a - j\delta|a|^2 a. \qquad 2.4.12$$

When dispersion *(D)* is negative, the pulse distortion due to the nonlinear chirp can be compensated and this results in the formation of soliton-like pulses where amplitude in the time domain is given by

$$a(T,t) = A_0 \mathrm{sech}\left(\frac{t}{\tau}\right) e^{-j\delta|A_0|^2 T/T_R}. \qquad 2.4.13$$

From Eq. 2.4.13, it is obvious that pulse profile of the generated pulses will exhibit hyperbolic secant distribution. The generated pulse energy is further given by

$$W = 2|A_0|^2\tau. \qquad 2.4.14$$

In addition, from the solution of the master equation (Eq. 2.4.12), it can be shown that the solution satisfies the area theorem

$$|A_0|\tau = \sqrt{\frac{2|D|}{\delta}}. \qquad 2.4.15$$

By squaring both sides and using Eq. 2.4.15, one obtains the relation between pulse energy (W), pulse duration divided by a factor of 1.76 (τ) and group velocity dispersion (D) as

$$W = \frac{4|D|}{\tau\delta}. \tag{2.4.16}$$

During pulsed operation initiated by the Kerr effect, the laser operates with a definite pulse energy, intracavity dispersion, and pulse duration. From the knowledge of all these parameter, one can use Eq. 2.4.16 to determine the nonlinear refractive index n_2 of the gain medium.

2.4.2 Group Velocity Dispersion (GVD)

As it is mentioned above, very precise dispersion management should be done to generate ultrashort pulses via KLM. An empirical relation called Sellmeier equation models the change of the refractive index with respect to wavelength. In our experiments, zinc selenide (ZnSe), and magnesium fluoride (MgF_2) materials were used. Their Sellmeier equations are [38]:

$$n(\lambda)_{\mathrm{ZnSe}} = \sqrt{9.01536 + \frac{0.24482}{\lambda^2 - 0.29934^2} + \frac{7229.931303}{\lambda^2 - 48.38^2}} \tag{2.4.17}$$

$$n_0(\lambda)_{\mathrm{MgF2}} = \sqrt{1 + \frac{0.48755\lambda^2}{\lambda^2 - 0.04338^2} + \frac{0.39875\lambda^2}{\lambda^2 - 0.09461^2} + \frac{2.312\lambda^2}{\lambda^2 - 23.794^2}}$$

$$n_e(\lambda)_{\mathrm{MgF2}} = \sqrt{1 + \frac{0.41344\lambda^2}{\lambda^2 - 0.03684^2} + \frac{0.50498\lambda^2}{\lambda^2 - 0.09076^2} + \frac{2.4905\lambda^2}{\lambda^2 - 23.772^2}}$$

$$n(\lambda)_{\mathrm{MgF2}} = \sqrt{\frac{2}{3}n_0(\lambda)^2_{\mathrm{MgF2}} + \frac{1}{3}n_e(\lambda)^2_{\mathrm{MgF2}}} \tag{2.4.18}$$

respectively. In Fig. 2.4.5, calculated variation of the refractive index with respect to wavelength between 2.2 to 2.6 μm is shown for ZnSe and MgF_2.

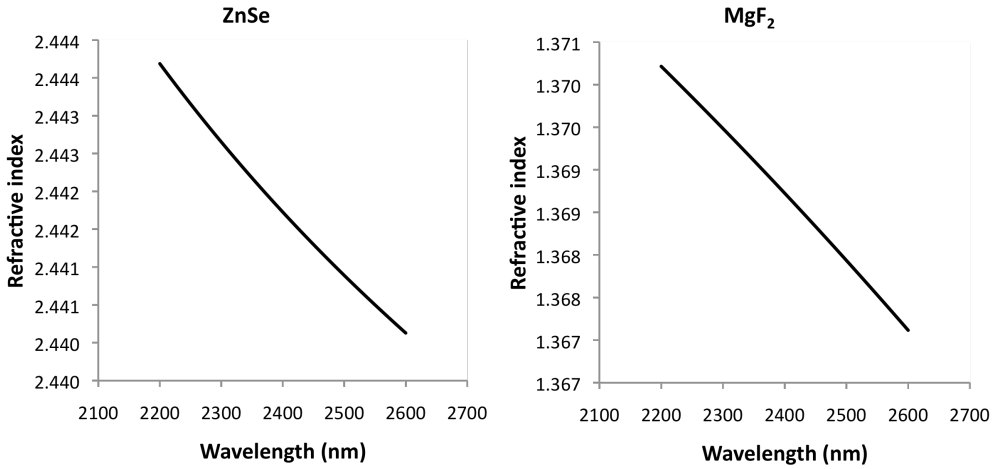

Figure 2.4.5: Wavelength dependence of refractive index for polycrystalline ZnSe and MgF_2.

Therefore, when a pulse, which is formed by several spectral components, meets a material interface, each spectral component refracts with different angles (See Fig. 2.4.6).

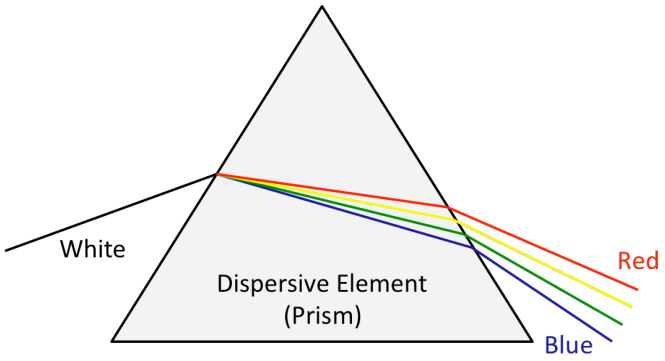

Figure 2.4.6:Schematic illustration of white light passing through a prism

Group velocity dispersion (GVD) for a slab of material is formulated as the second derivative of the phase with respect to frequency as [39]

$$\frac{\mathrm{d}^2\varphi}{\mathrm{d}\omega^2} = \frac{\lambda^3 L_S}{2\pi c^2}\frac{\mathrm{d}^2 n}{\mathrm{d}\lambda^2}, \qquad 2.4.19$$

in which φ is the phase, ω is the angular frequency, L_S is the length of the slab, c is the speed of light and n is the refractive index. The sign of the GVD is governed by the second

derivative of the refractive index. In Fig. 2.4.7, $d^2n/d\lambda^2$ for ZnSe is positive where $d^2n/d\lambda^2$ for MgF_2 is negative.

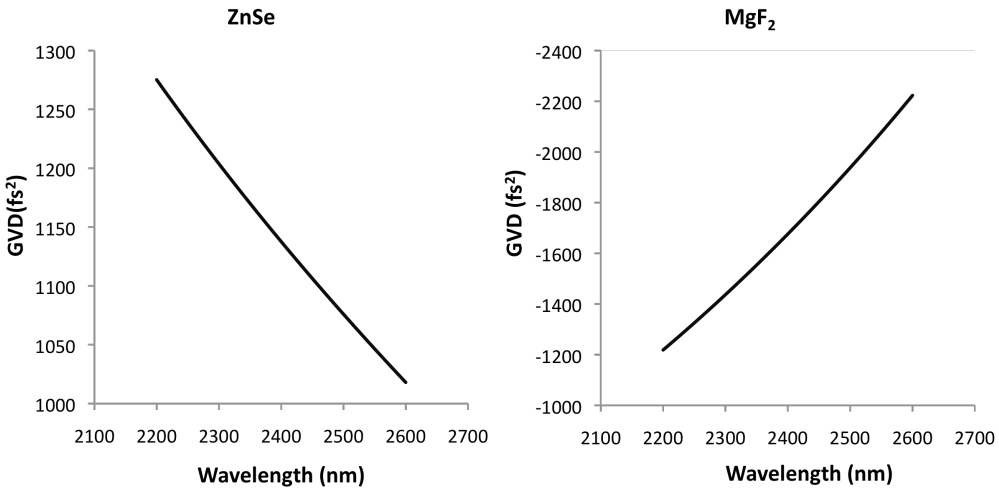

Figure 2.4.7: Variation of second order GVD as a function of wavelength.

Another way of producing negative GVD is by employing a prism pair configuration that is illustrated in Fig. 2.4.8. According to Fork et al [39], GVD generated from a prism pair is

$$\frac{\mathrm{d}^2\varphi}{\mathrm{d}\omega^2} = \frac{\lambda^3}{2\pi c^2}\frac{\mathrm{d}^2 Z}{\mathrm{d}\lambda^2}, \qquad 2.4.20$$

where Z is the optical path and the second derivative of optical path with respect to wavelength is defined as

$$\frac{\mathrm{d}^2 Z}{\mathrm{d}\lambda^2} = 4\left[\frac{\mathrm{d}^2 n}{\mathrm{d}\lambda^2} + (2n - n^{-3})\left(\frac{\mathrm{d}n}{\mathrm{d}\lambda}\right)^2\right] L_P \sin\beta - 8\left(\frac{\mathrm{d}n}{\mathrm{d}\lambda}\right)^2 L_P \cos\beta \qquad 2.4.21$$

here L_P is the separation between the apices of the prism pair and β is the angular spread in the beam due to dispersion.

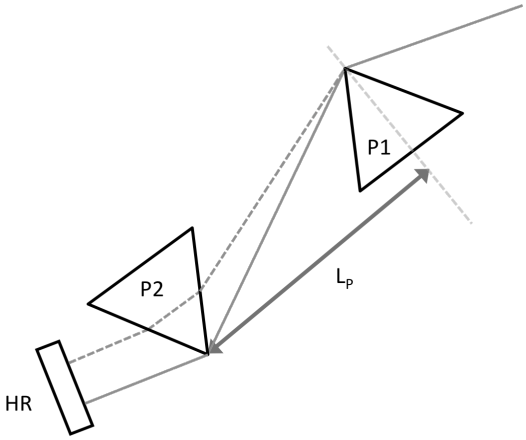

Figure 2.4.8: A typical prism pair configuration to produce negative GVD.

By using these design equations, GVD values of 2.4-mm-long ZnSe gain crystal, L_P=8.5cm spaced prism pair and the insertion (L_S=9.2mm) of the MgF_2 prisms were calculated. Wavelength dependence of calculated total GVD is given in Fig. 2.4.9.

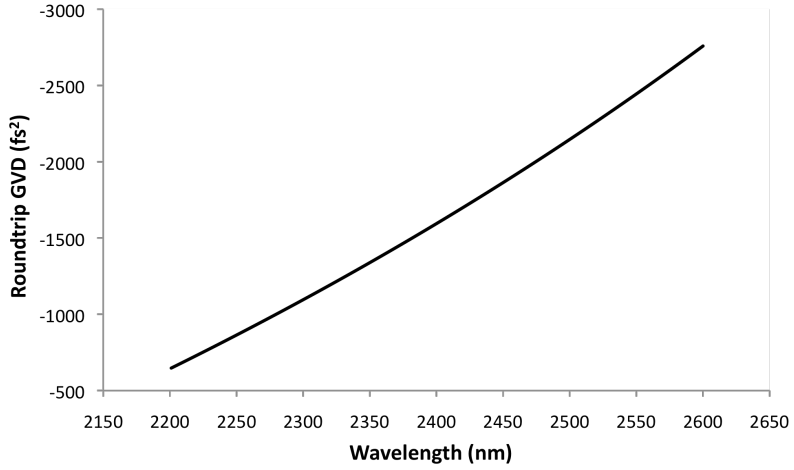

Figure 2.4.9:Estimated total roundtrip GVD of resonator as a function of wavelength.

As was mentioned in our earlier discussion on KLM, Haus et al [17] predicted that without negative GVD, a soliton cannot be formed. As a result, in our experiments, a prism pair (See Fig. 2.4.8) was used as a negative GVD source which always generates negative GVD.

Chapter 3: Experimental Results

In this chapter, continuous-wave (CW) and mode-locked regimes of the Cr:ZnSe laser will be characterized in detail. In the first section, the elements of the laser, which are the pump source, the gain medium, and the resonator, will be introduced. Continuous-wave power performances of three samples will be discussed. In the second section, mode-locked operation of the laser will be described in detail by including the generated pulse profile, the spectrum of the pulses, as well as the estimation of the nonlinear refractive index for ZnSe.

3.1 Continuous-Wave Characterization

A linearly polarized 5W Tm-fiber laser (IPG Photonics, TLR-5-1800-LP) operating at 1800 nm was used as the pump source. It was focused with a 10-cm input lens (L1) inside the Cr:ZnSe crystal. A standard, astigmatically compensated, asymmetric x cavity was used in the experiments. In Figs. 3.1.1 and 3.1.2 the schematic and picture of the experimental setup can be seen. The resonator included two curved dichroic high reflectors (M1 and M2), each with radius of 100 mm, a flat high reflector (HR) and a flat output coupler (OC). The curved mirrors M1 and M2 are highly reflecting at the laser wavelength of 2.5 μm and highly transmitting at the pump wavelength of 1.8 μm. The crystal was placed at Brewster

angle to reduce reflection losses, and it was attached with indium foil between copper plates that were water cooled at 21 °C. In Figs. 3.1.1 and 3.1.2, dark colored trace indicates the path of the pump beam where light colored trace shows the path of the laser beam traveling inside the resonator.

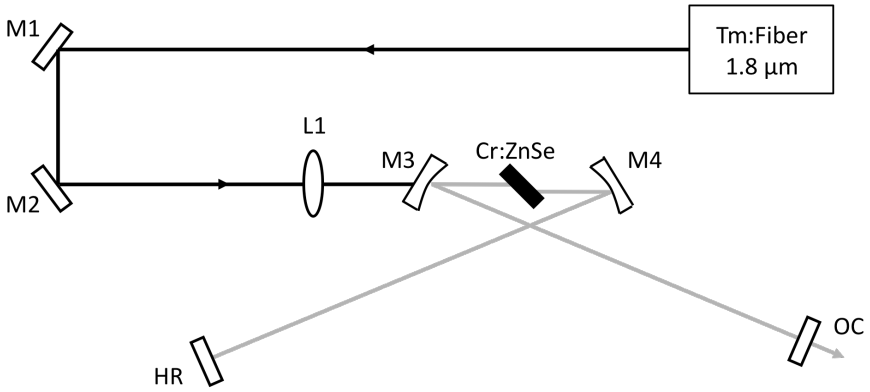

Figure 3.1.1: Schematic of the continuous-wave Cr:ZnSe laser.

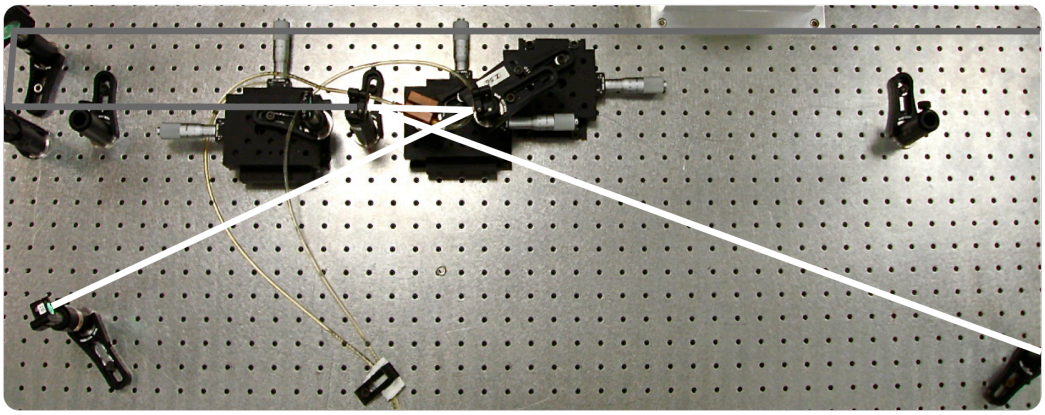

Figure 3.1.2: Digital image of the continuous-wave Cr:ZnSe laser.

In cw experiments, three samples were investigated to determine which one delivers the highest cw power. In Table 3.1.1, some important parameters of the samples are summarized. One of the samples was a 5-mm-long, diffusion doped sample prepared in our laboratories. It was kept in the furnace at 1000°C for 2.5 days. According to summarized

values in Table 3.1.1, poor power performance of the homemade sample is mainly due to the poor surface quality. In the case of sample 1 and 3, as you see, the absorption coefficient of the sample 1 is almost 2.5 times greater than that of sample 3, which allows the highest continuous wave output power.

Sample 1	**Sample 2**	**Sample 3**
Commercial sample (Spectragen, Inc) Length: 2.4 mm Cr^{2+} Concentration: $10.1x10^{18}$ cm^{-3}	Homemade sample (T@1000°C, 2.5 days) Length: 5 mm Cr^{2+} Concentration: $5.2\ x10^{18}$ cm^{-3}	Commercial sample (Photonics Innovations) Length: 2.6 mm Cr^{2+} Concentration: $4.1\ x10^{18}$ cm^{-3}
@1.8 μm Absorbed Power: 94% of incident pump power Absorption Coefficient: 11.6 cm^{-1}	@1.8 μm Absorbed Power: 95% of incident pump power Absorption Coefficient: 6.0 cm^{-1}	@1.8 μm Absorbed Power: 70% of incident pump power Absorption Coefficient: 4.7 cm^{-1}
Continuous-Wave Output Power: 140 mW Pump Power: 960 mW	Continuous-Wave Output Power: 13 mW Pump Power: 960 mW	Continuous-Wave Output Power: 96 mW Pump Power: 960 mW

Table 3.1.1: Comparison of some important parameters between investigated samples.

As it can be seen from the Table, sample 1 was 2.4 mm long, and it absorbs 94% of incident power at 1800 nm with corresponding pump absorption coefficient of 11.6 cm^{-1}. The laser was operated with two different output couplers having 1% and 6% transmission at 2400 nm.

Power performance of both configurations is shown in Fig. 3.1.3. The highest output power of 405 mW was obtained by using the 6% output coupler with corresponding intracavity laser power of 6.75W. The corresponding slope efficiency was 2.4%. With the 1% output coupler, the highest output power obtained was 150mW which corresponds to 15W with a slope efficiency of 7.9%. By lowering the output coupling level, the intracavity power increased dramatically, which is more favorable in the case of mode locking experiments.

From the slope efficiency data, the total round-trip passive loss of the crystal (Eq. 2.3.13) and the resonator optics was estimated to be 3.65 %.

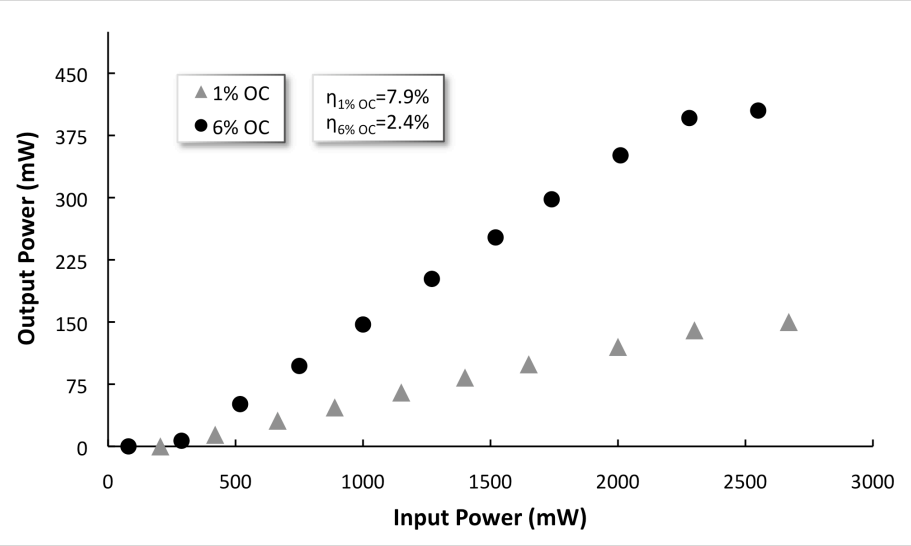

Figure 3.1.3: Continuous-wave efficiency curve taken with 1% and 6% output couplers and sample 1.

The total cavity length was 159 cm, with asymmetric high reflector and output coupler arm lengths of 66 cm and 83cm, respectively. By using the ABCD matrix analysis described in Section 2.2.2, the beam waist inside the crystal was estimated to be 32μm, with a root mean squared value $(\omega_0)_{rms}$ of 34 μm.

3.2 Mode-Locked Characterization

In Kerr-lens mode locking experiments, dispersion compensation was provided with a MgF_2 prism pair. As seen in Fig. 3.2.1, it was placed on the high reflector arm (P1 and P2 in Fig. 3.2.1). The tip-to-tip separation between the prisms was adjusted to be 8.5 cm and each prism was placed at minimum deviation. The cw power efficiency curve with the prism pair is shown in Fig. 3.2.2. After the addition of the prism pair to HR arm as seen in Fig 3.2.1, cavity roundtrip loss increased to 7.3%.

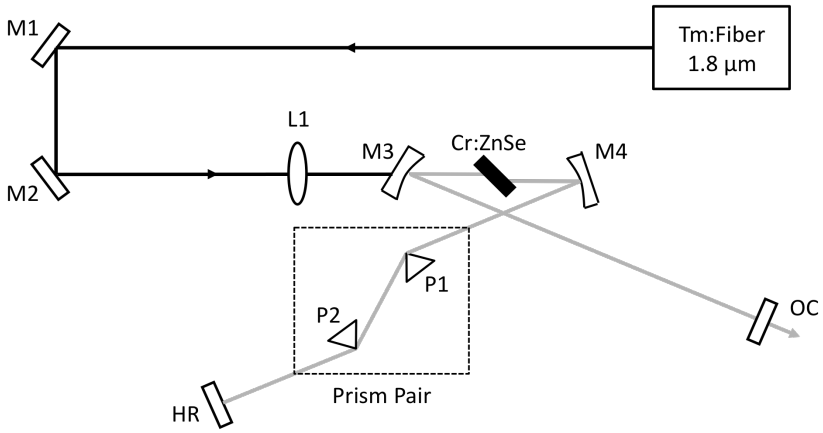

Figure 3.2.1: Schematic of mode-locked operating Cr:ZnSe laser.

Based on the cw power efficiency curve in Fig. 3.2.2, the highest power delivered from the laser was reduced to 100mW, and the corresponding intracavity power decreased to 10W. As a result, the slope efficiency became 4%. The loss is mainly due to the imperfect surface quality of the prisms.

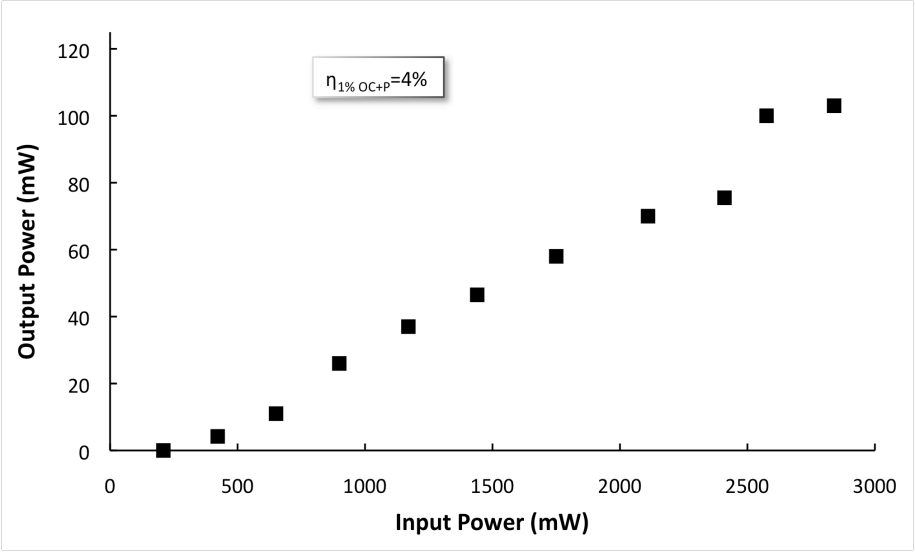

Figure 3.2.2: The efficiency curve which was taken with the prism pair and 1% OC.

To estimate the net dispersion of the cavity [39] (Also see Section 2.4.2 for details), the dispersion contribution due to the prism insertion, prism pair, and ZnSe gain medium were taken into account. Summary of calculated values at 2.42 μm can be found in Table 3.2.1.

	ZnSe	Prism insertion	Prism pair	TOTAL
GVD(fs^2)	1125	-1726	-1099	-1700
Thickness (mm)	2.4	9.2	L_P=8.5cm	-

Table 3.2.1: Calculated GVD values for three dispersion sources based on the article of Fork et al. [39] .

Once the focusing inside the gain medium was optimized by adjusting the positions of the curved high reflectors M1 and M2, stable, Kerr-lens mode-locked operation could be initiated by translating the output coupler. In fact, several conditions had to be met in order to initiate mode-locked operation. First, the intracavity power had to be sufficiently high. In the experiments, KLM action could be obtained only with the 1% output coupler. Second, mode-locked pulse train could be more readily initiated by maintaining an asymmetric arm ratio. In particular, increasing the high reflector arm length beyond 70cm, we could not initiate mode-locked operation despite the fact that pulse energy became somewhat larger compared to the 94 MHz cavity.

The generated pulses from the Cr^{2+}:ZnSe laser was characterized with a mid-infrared autocorrelator and a home-made mid-infrared scanning spectrometer (See Appendix A-B for details of the setups). The collinear autocorrelation signal was registered via two-photon absorption current induced in a germanium detector. From the autocorrelation measurement, the pulsewidth (FWHM) was determined to be 95-fs by assuming a $sech^2$ pulse profile as seen in Fig. 3.2.3.

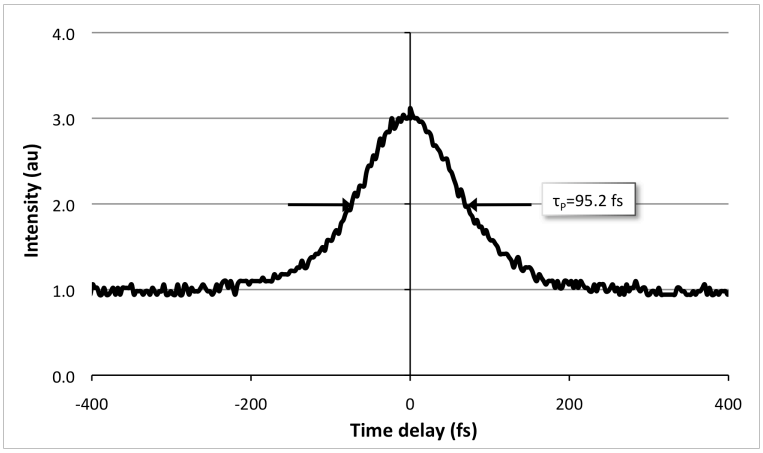

Figure 3.2.3: Autocorrelation trace of the generated pulses, the pulsewidth was measured to be 95fs by assuming a $sech^2$ shaped pulse profile.

The output spectrum had a width of 69nm, and Kelly sidebands were formed at both sides of the central wavelength as seen in Fig. 3.2.4. These peaks occur when the soliton encounters periodical perturbations in the gain, loss, filtering and the self amplitude modulation (SAM) action. As a result, soliton radiates and drains the pulse energy to these side bands. Theoretically, they must be symmetric but in our experiments, we observed that they were not. It is mainly due to the presence of third-order dispersion in the resonator [40].

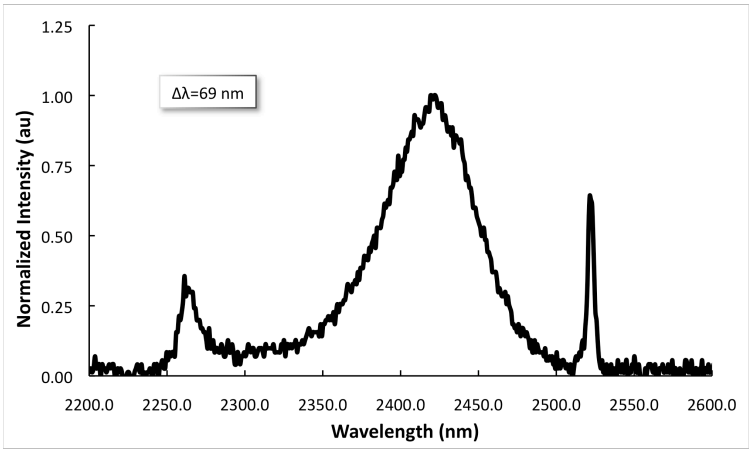

Figure 3.2.4: The spectrum of the mode-locked pulses.

The time-bandwidth product was calculated as 0.335, and it is close to the transform-limited value of 0.315 (See Eq. 2.4.7). The spectrum and the pulse profile were recorded simultaneously.

The mode-locked output power and the pump power were 40mW and 2.1W, respectively. Cavity length was 159 cm, so the repetition rate of the pulse train was 94.3 MHz. The peak power and the pulse energy of the pulses were 4.2kW and 0.42nJ, respectively.

Based on the soliton area theorem introduced in Section 2.4.1, the nonlinear refractive index of the Cr:ZnSe crystal is calculated [41]. From Eq. 2.4.16,

$$W = \frac{4|D|}{\tau\delta}. \tag{3.2.1}$$

Here τ is pulsewidth divided by a factor of 1.76. The Kerr nonlinear coefficient was calculated as

$$\delta = \frac{4|-1700\times10^{-30}|}{(54.1\times10^{-15})(42\times10^{-9})} \tag{3.2.2}$$

giving,

$$\delta = 0.33\times10^{6}\mathrm{W}. \tag{3.2.3}$$

Now, that the Kerr coefficient is known, n_2 can be calculated by using Eq. 2.4.10:

$$\delta = \frac{2\pi n_2 L_C}{\lambda_0 A_{eff}}. \tag{3.2.4}$$

Above, n_2 is the nonlinear refractive index, L_C is the length of the nonlinear medium, λ_0 is the central wavelength, and A_{eff} is the effective area. As a result, the nonlinear refractive index was calculated from

$$n_2 = \frac{(0.33 \times 10^6)(2.42 \times 10^{-6})(3.18 \times 10^{-9})}{2\pi(2.59 \times 10^{-3})}, \quad 3.2.5$$

resulting in

$$n_2 = 1.4 \times 10^{-14} \mathrm{cm}^2/\mathrm{W}. \quad 3.2.6$$

The calculated value of n_2 agrees well with the previously reported value of 1.7×10^{-14} cm^2/W for Cr^{2+}:ZnSe [42]. It is almost 100 times larger than the n_2 of the sapphire [13]. As a result, in the case of Cr:ZnSe laser, to balance the nonlinear chirp created by the Kerr effect, more negative GVD is required in comparison with Ti:Sapphire lasers.

Chapter 4: Stretcher and Compressor Design

We aimed at building a chirped pulse amplifier (CPA), to amplify the peak powers of the generated seed pulses. It includes three main stages. The first phase is the stretching of seed pulses. In the second phase, stretched pulses will be injected into a gain-switched Cr:ZnSe laser for amplification. In the third phase, amplified pulses will be compressed to the initial pulse duration. In this chapter, the stretcher and the compressor designs will be described.

To stretch or compress the pulse durations from femtoseconds to picoseconds and back, large amount of group velocity dispersion (GVD) are required. According to Fork et al [39], a prism pair or a grating pair can be used to provide GVD. But compared to a prism pair, grating pair generates more GVD and the sign of the required dispersion can be adjusted as well. As a result, grating pair is preferred as the dispersion source in our design.

4.1 Stretcher Design

4.1.1 Diffraction Grating

Diffraction grating is an optical device, which separates the incident light into its spectral components. There is a repeating groove pattern engraved on its surface. In order to observe the diffraction phenomena, the dimensions of the pattern should be close to the

wavelength of light. In Fig. 4.1.1, a reflecting diffraction grating is illustrated. White light falls on it with an angle of incidence equal to α.

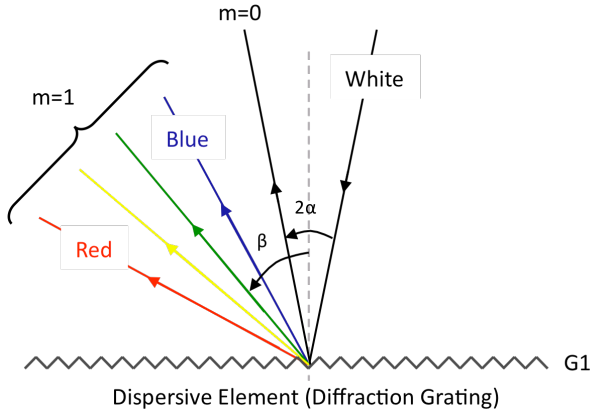

Figure 4.1.1: A reflecting diffraction grating, and the illustration of diffraction.

Zeroth order diffraction again occurs at an angle α, but on the other side of the normal. First order diffraction angle, β, is a function of wavelength. The relation between the diffraction angle and the wavelength is

$$\sin\alpha + \sin\beta = m\lambda g_D \qquad 4.1.1$$

and it is called the grating equation. Here α is the angle of incidence, β is the angle of diffraction, g_D is the groove density, m is the order of diffraction, and λ is the wavelength.

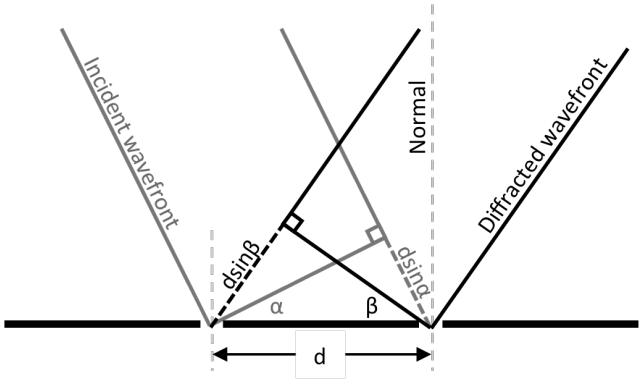

Figure 4.1.2: Wavefronts of diffracted light.

More detailed representation of diffraction is illustrated in Fig. 4.1.2 by taking into account the wave property of light. In order to obtain constructive interference from the consecutive grooves, the path difference should be equal to an integer times the wavelength. This results in

$$d\sin\alpha + d\sin\beta = m\lambda. \qquad 4.1.2$$

Here d is the groove spacing. The inverse of the groove spacing equals the groove density $g_D=1/d$, and m is an integer that describes the order of diffraction. Eq. 4.1.2 is equivalent to the grating equation in Eq. 4.1.1.

There are two possibilities for the diffraction direction:

1) If the calculated diffraction angle is positive, then the angle of incidence and the angle of diffraction are on the same side of the normal.
2) If the calculated diffraction angle is negative, then the angle of incidence and the angle of diffraction are on the opposite side of the normal.

Grating pair adds extra chirp to pulses, so that the pulse durations become larger. In Fig. 4.1.3, the effect of negative and positive group velocity dispersion on a pulse is illustrated.

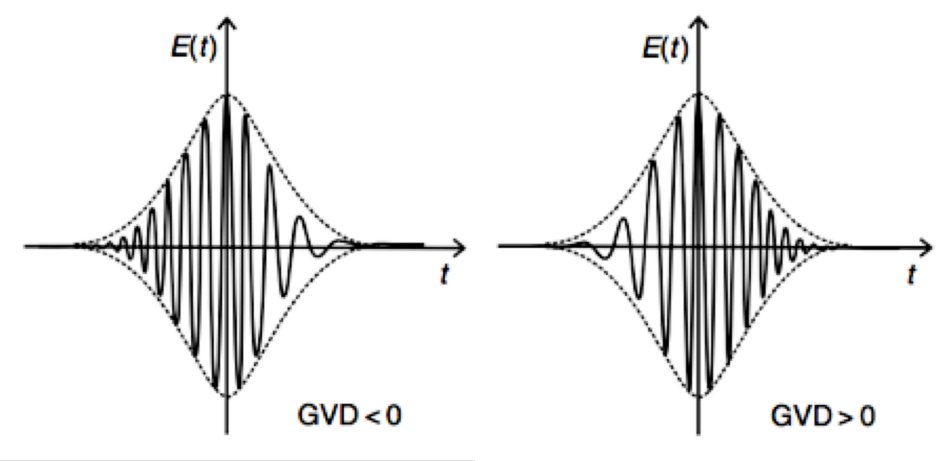

Figure 4.1.3: Positive and negatively chirped Gaussian pulses.

In the case of the stretcher design, the initial and final pulse durations are determined by the seed and gain switched laser, respectively. For a Gaussian pulse profile, the required amount of dispersion for stretching can be calculated from

$$\tau_f = \tau_0 \sqrt{1 + \left(\frac{4D \ln 2}{\tau_0^2} \right)^2}, \qquad 4.1.3$$

where τ_f is the final pulsewidth, τ_0 is the initial pulsewidth and D will be the required amount of dispersion.

There are two configurations which can be used as stretcher or compressor. However, practically only one of them can be used as a stretcher. One of the configurations includes a focusing element to invert the order of spectral components, so that after the compression stage, high peak powered pulses may damage the gratings. As a result, the following configuration is preferred as the stretcher (See Fig. 4.1.4).

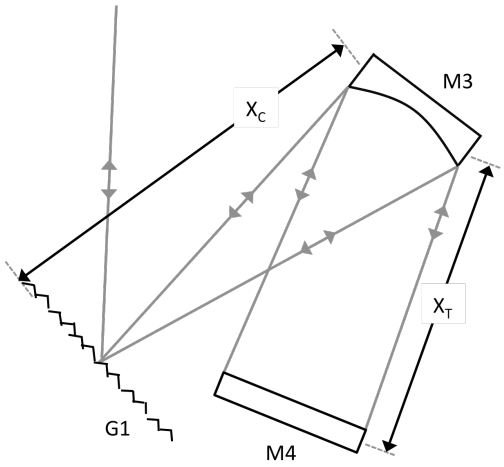

Figure 4.1.4: Intended stretcher design with only one grating [43].

For this configuration, the generated GVD can be calculated by using [43]

$$D = -\frac{g_D^2 \lambda^3}{2\pi c^2 \cos^2 \beta} 2\mathrm{Z}, \qquad 4.1.4$$

where λ is the wavelength, g_D is the groove density, β is the angle of diffraction, Z is defined as the optical path relative to the focal length of the concave mirror (M3). In Fig. 4.1.4 when the distances X_C and X_T are both equal to the focal length of the concave mirror (M3), the system will have net zero GVD. On the other hand, if the distance X_C is extended beyond the focal length of the M3, then negative GVD will be generated. Also, setting X_C smaller than the focal length of M3 will generate positive GVD. As you can see, desired sign and amount of dispersion can be selected by simply adjusting the distances X_C and X_T.

Above design equations were applied to a diffraction grating which has a blaze angle of 17.5°, groove density of 300 g/mm and optimized to a wavelength of 2000 nm. First, the required amount of GVD for stretching was calculated by using Eq. 4.1.2 in the form

$$100 \times 10^{-12} = 100 \times 10^{-15}\sqrt{1 + \left(\frac{4\mathrm{D}\ln 2}{(100 \times 10^{-15})^2}\right)^2}, \tag{4.1.5}$$

yielding

$$\mathrm{D} = \pm 3.61 \times 10^{6}\mathrm{fs}^2. \tag{4.1.6}$$

Here τ_f and τ_0 are assumed to be 100ps and 100fs, respectively. In order to reach to the calculated GVD value (D), diffracted angle was calculated via Eq. 4.1.1 as

$$\sin 28^\circ + \sin\beta = (2400 \times 10^{-9})(300 \times 10^{3}) \tag{4.1.7}$$

$$\beta = -41.85^\circ. \tag{4.1.8}$$

Here the angle of incidence is 10 degrees deviated from the blaze angle, in order to avoid Littrow configuration (i.e, angle of diffraction and incidence happens to be the same). The required distance, Z, was calculated via Eq. 4.1.3 for Fig. 4.1.4 from

$$\pm 3.61 \times 10^{-24} = -\frac{(300 \times 10^{3})^2(2450 \times 10^{-9})^3}{2\pi(3 \times 10^{8})^2\cos^2(-41.85^\circ)}2\mathrm{Z}, \tag{4.1.9}$$

giving

$$Z = \pm 76.8\text{cm}. \qquad 4.1.10$$

The sign of distance is directly related to the desired sign of GVD. In our design, we preferred to add positive GVD in stretcher phase. As a result, based on our calculations, X_T and X_C should be -76.8cm shorter than the focal length of the curved mirror (M3) in Fig. 4.1.4. If a prism pair was used instead of a grating pair, the distance between the prisms would be 0.3 km whereas with the grating pair only 0.77 m of separation is enough to generate the same amount of GVD.

4.2 Compressor Design

After the amplification phase, amplified picosecond pulses will be compressed back to the initial pulse duration of 100fs. In the earlier section, positive GVD was preferred for the stretching phase. To cancel the effect of positive GVD, pulses should now acquire negative GVD.

The simplest configuration to apply negative GVD without focusing is illustrated in Fig. 4.2.1.

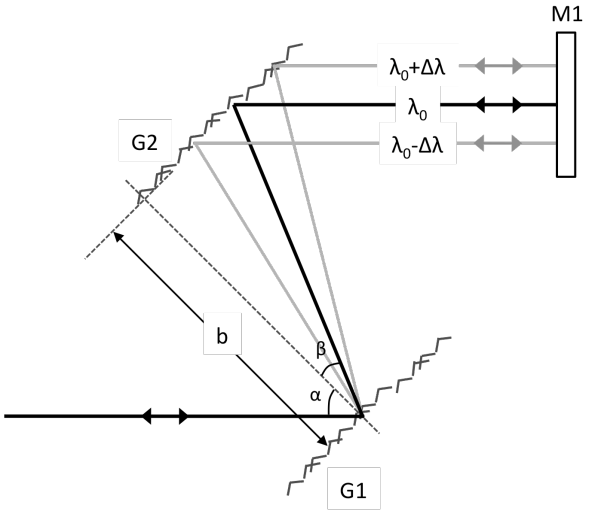

Figure 4.2.1: Desired grating pair configuration for pulse compression.

In this configuration, when positively chirped pulses pass through the grating pair, previously added positive chirp is removed, and pulses compressed to initial pulse durations. In ref: [44], the second order GVD expression of the above grating pair is given as

$$D = -\frac{\lambda^3}{2\pi c^2}\frac{g_D^2 b}{\cos^3\beta}. \qquad 4.2.1$$

Here, λ is the wavelength, g_D is the groove density, b is the normal distance between the grating pair and β is the diffracted angle. In Fig. 4.2.1, λ_0 represents the center wavelength of the pulse and the reason why we put the mirror M1 to the output of the grating pair is not trivial. From the Fig. 4.2.1, it is clear that, after passing the grating pair once, each spectral component diffracts to different directions. When it reflects back and passes once more from the grating, the spectral dispersion disappears and only the contribution of negative GVD stays. In conclusion to provide negative GVD, pulses should pass two times from the grating pair. There is one more configuration including only one diffraction grating which is illustrated in Fig. 4.2.2.

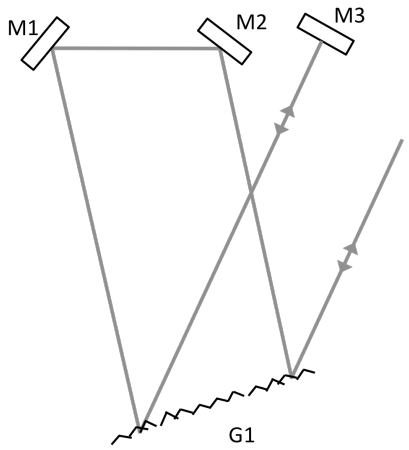

Figure 4.2.2: Equivalent compressor configuration of simple grating pair illustrated in Fig. 4.2.1.

Note that in Eq. 4.2.1 b was defined as the normal distance between the gratings, but for the configuration in Fig. 4.2.2 other than the normal distance, optical path becomes important. The relation between the normal distance (b) and the optical path (L_G) is

$$b = L_G \cos\beta. \tag{4.2.2}$$

Remember that here, β was the diffraction angle. When the above relation is plugged into Eq. 4.2.1, the following relation is obtained for GVD once more:

$$D = -\frac{\lambda^3}{2\pi c^2}\frac{g_D^2 L_G}{\cos^2\beta}. \tag{4.2.3}$$

This result is for the compressor configuration illustrated in Fig. 4.2.2. In the previous section beginning from Eq. 4.1.7 to Eq. 4.1.10, we already calculated the required optical path and found that it should be 76.8cm. The same procedure holds for the compressor calculations as well. If the distances in Fig. 4.2.2 are precisely adjusted to a total of 76.8cm, then the correct amount of negative chirp will be supplied and the resulting pulse durations will be shortened to the initial values.

Chapter 5: Conclusions

In this thesis work, development of a seed laser and a stretcher compressor design were described, which are the three basic elements of a chirped pulse amplifier (CPA).

In the case of the seed laser, a Kerr lens mode-locked Cr^{2+}:ZnSe was constructed. An astigmatically compensated, asymmetric x-cavity containing a 2.4-mm-long Cr^{2+}:ZnSe sample with a pump absorption coefficient of 11.6 cm^{-1} was used. It operated with a 1% output coupler. Dispersion compensation was achieved by using a MgF_2 prism pair, separated by 8.5 cm distance. During Kerr lens mode locking (KLM), the total group velocity dispersion (GVD) was calculated to be -1700fs^2 by taking into account the crystal, prism insertion and the prism spacing. During Kerr-lens mode-locked operation, 95-fs pulses at a pulse repetition rate of 94.3 MHz were generated with 40 mW of output power. The center wavelength of the pulses was 2.42 μm with a spectral width of 69 nm. Corresponding time-bandwidth product was 0.335, which is close to the transform limit for hyperbolic secant pulses. In addition, by using the soliton area theorem, the estimated value of the nonlinear refractive index came to

$1.4x10^{-14}$ cm^2/W for Cr^{2+}:ZnSe, which agrees well with previously reported results. Note also that the effective n_2 for Cr:ZnSe is approximately 100 times larger than that for Ti:Sapphire. Mid-infrared femtosecond pulses in the 2-3 μm range should find numerous applications in high harmonic generation, metrology, and spectroscopy.

In the case of stretcher and compressor design, we calculated the required GVD values to stretch and compress 100 femtosecond pulses to 100 picoseconds. Since the required GVD values are so large, of the order of 10^6 $fsec^2$, a grating pair was preferred instead of a prism pair. For the stretching step, positive chirp will be added by using a focusing element to invert the order of spectral components. The stretched pulse will overlap better with the amplifier pulses, and then it will be compressed by the compressor. For the compression stage, a simple configuration is preferred to avoid possible damages that can be caused by the high power pulses to gratings. In addition, it will just provide the same amount of negative GVD to remove initially added chirp to the pulses. In conclusion, the total optical path between the grating pairs is calculated as 2x76=152 cm. If we had used a prism pair, then the distance between the prism pair would be 0.3 km which is practically impossible to build in a lab environment.

Appendix A: Mid-IR Scanning Spectrometer

During the mode locking experiments, one needs to monitor the pulse train or the spectrum of the output pulses to confirm that the laser operates in mode-locked regime. When the laser operates in CW regime, the width of the spectrum is typically less than the resolution of the spectrometer. However, when femtosecond pulses are generated, the spectrum of the pulses expands dramatically. For example in our experiments, the spectral width of the pulses was 69nm. As a result, with a high-resolution spectrometer, it is easy and reliable to determine the mode-locked regime of the laser. When the output of the laser is monitored with a slow detector, one may get confused by random oscillations of the laser and cannot precisely diagnose the mode locked operation. As a result, during the experiments, it is more practical to use a scanning spectrometer instead of monitoring the pulse train. Commercially available real time spectrometers typically cover the visible and near infrared regions of the spectrum. Moreover, beyond 2 μm, the linewidth of commercial scanning spectrometers increases up to 50-60 nm, which makes it impossible for us to distinguish the cw and mode-locked regimes of the laser.

Because of all these facts, a high-resolution Mid-IR scanning spectrometer was needed to diagnose the mode-locked operation. A spectrometer was constructed by Adnan Kurt from Teknofil Inc. to monitor the 1.8-2.8 μm wavelength range with a resolution of less than 2 nm.

The design includes two phases. The first one was the optical part including the steering and focusing mirrors which aim the light first to diffraction grating and then to the detector. In this respect, the well-known Czerny-Turner monochromator configuration was used. The configuration includes two concave mirrors and one flat diffraction grating. In addition to that, an adjustable aperture and a flat metallic mirror are used as well. A schematic and digital image of the spectrometer can be seen in Figs. A1 and A2, respectively.

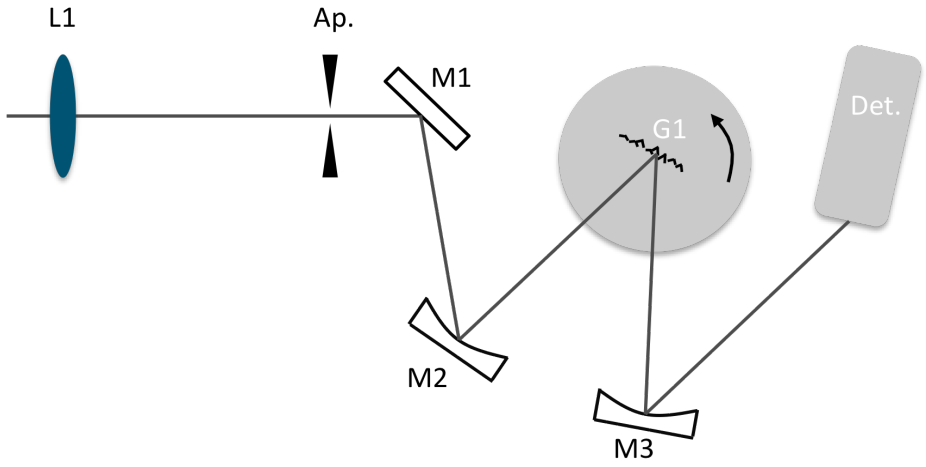

Figure A1: Schematic illustration of the scanning mid-IR spectrometer.

In Fig. A1, L1 is the input lens that focuses the incident light through the aperture (entrance slit), and M1 aims the light to the scanning spectrometer. The concave metallic mirror (M2) focuses the light onto reflecting diffraction grating (G1). The diffracted light coming from the grating is focused with the second concave metallic mirror (M3) on to the detector. Because of small active area of the detector, it is used as the exit slit of the CT monochromator setting. When the grating was rotating, at each instant of time, a different

spectral component of the pulse will be focused onto the detector. An InGaAs photo diode (Bandwidth= 60 MHz) was used to monitor the spectrum which was terminated by 50Ω.

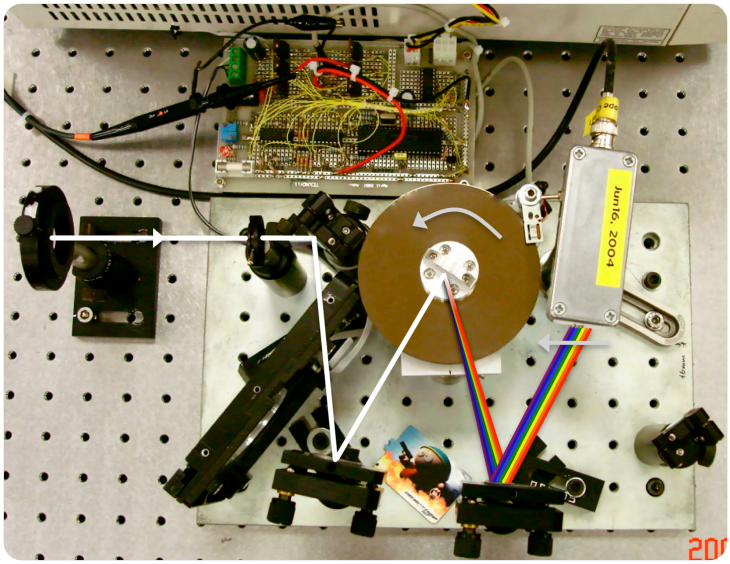

Figure A2: Digital image of the homemade mid-IR scanning spectrometer.

The observable spectrum range is limited by the spectral bandwidth of the detector. Photosensitivity versus wavelength plot of the detector is seen in Fig. A3. Beginning from 1.9 μm and up to 2.4 μm, it is flat. However, at 2.6 μm it drops to 20% of the initial value.

As we mentioned earlier, to enable real time monitoring, grating rotates around the center axis of the disc as shown in Fig. A2. In this respect, a brushless DC motor delivered a vibration free, uniform rotation to the disc, as well as the grating. The rotation speed was 7200 rpm and the period of the rotation was 41.67μs/°. The grating was a reflecting ruled grating with a groove density of 600g/mm, blaze angle of 28° 41', and it is optimized for the wavelength of 1600nm.

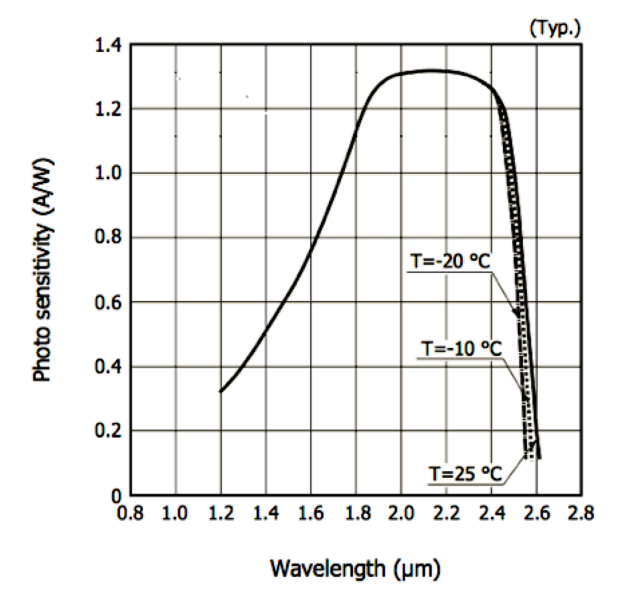

Figure A3: Wavelength response of the extended InGaAs photodiode.

After all the technical arrangements, now the spectrometer has to be calibrated which is the second phase of the design. The laser was tuned with a prism and the wavelength was measured with the CVI monochromator. At the same time, the corresponding time delay (*t*) (See Fig. A4) between peaks of zeroth and first order diffraction was recorded.

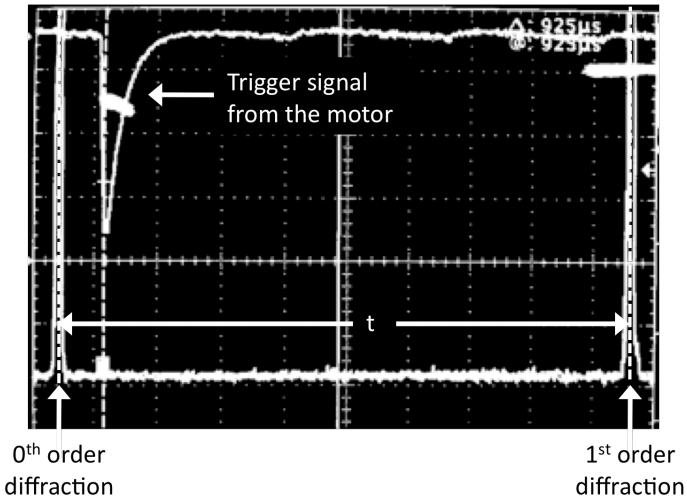

Figure A4: A typical oscilloscope screen of the home made spectrometer.

In Fig. A5, the recorded data are shown, and a 3rd order polynomial fit was done to convert delay values to wavelength. Obtained calibration fit is

$$\lambda = 4.992t^3 - 275.74t^2 + 1917.6t - 491.46 \qquad \text{A.1}$$

here *t* is the time delay that can be measured either on the oscilloscope by the help of the cursors or more practically it can be recorded by the computer.

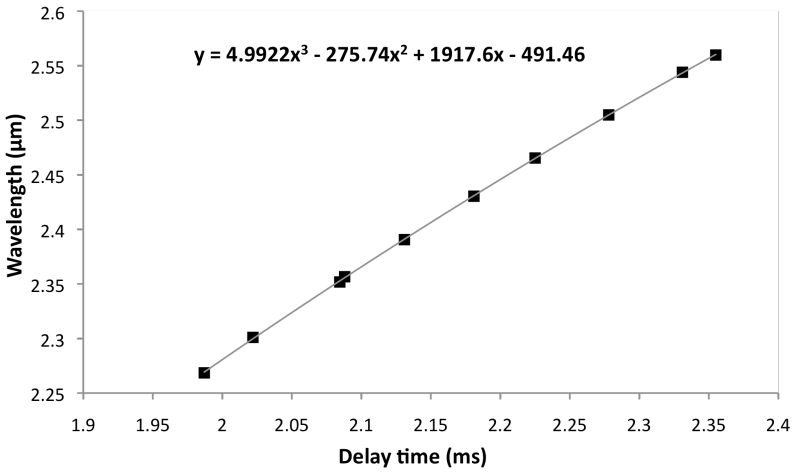

Figure A5: Calibration data taken with CVI monochromator and the scanning spectrometer.

Appendix B: Autocorrelator

The commercially available detectors and oscilloscopes are not able to measure the duration of femtosecond pulses. Therefore, in order to measure the pulse durations of the generated ultrashort pulses (95 fs), an intensity autocorrelator is established.

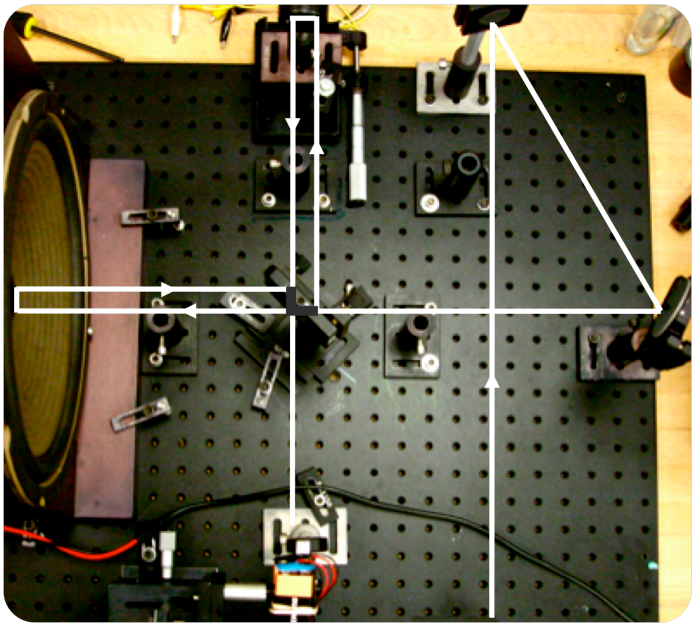

Figure B1: Digital image of the autocorrelator that we used to measure the pulse durations.

A typical intensity autocorrelator includes a Michealson interferometer and a semiconductor detector attached to the output of the interferometer as seen in Fig. B2. The digital image can be seen in Fig. B1.

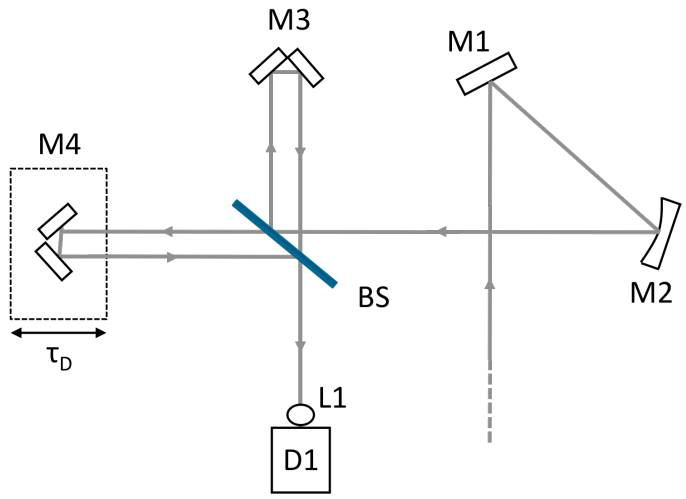

Figure B2: Schematic illustration of the intensity autocorrelator.

From Fig. B2, the beam splitter (BS) divides the incident pulse into two pulses. One travels to corner cube mirror M3, and the other goes to the other corner cube mirror M4, which is driven by a signal generator. Those divided pulses are recombined on the BS and focused onto a germanium (Ge) detector (D1) with the ball lens (L1). Since the Ge detector is not sensitive to 2.5 μm, it will only register the two-photon absorption signal. The generated two-photon absorption intensity profile will be proportional to [45]

$$I_{2P}(\tau_D) \sim \langle I^2(t)\rangle + \langle I^2(t-\tau_D)\rangle + 4\langle I(t)I(t-\tau_D)\rangle \qquad \text{B.1}$$

here τ_D is the delay time created by the movement of the corner cube mirror M4 in Fig. B2. Now both sides of Eq. B1 will be divided by $\langle I^2(t)\rangle$. Also $\langle I^2(t)\rangle = \langle I^2(t-\tau_D)\rangle$. As a result, the above equation becomes a function of

$$I_{2P}(\tau_D) \sim 1 + 2G^{(2)}(\tau_D) \quad \text{B.2}$$

where $G^{(2)}(\tau_D)$ is the second order autocorrelation function as a function of delay time (τ_D) and is given by

$$G^{(2)}(\tau_D) \equiv \frac{\langle I(t)I(t-\tau_D)\rangle}{\langle I(t)^2\rangle}. \quad \text{B.3}$$

When the generated pulses are coherent and well-behaved, we have

$$\frac{I_{2P}(0)}{I_{2P}(\tau_D \gg \tau_0)} = 3. \quad \text{B.4}$$

These results lead to an autocorrelation trace with a 3-to-1 ratio as seen in Fig. A3.

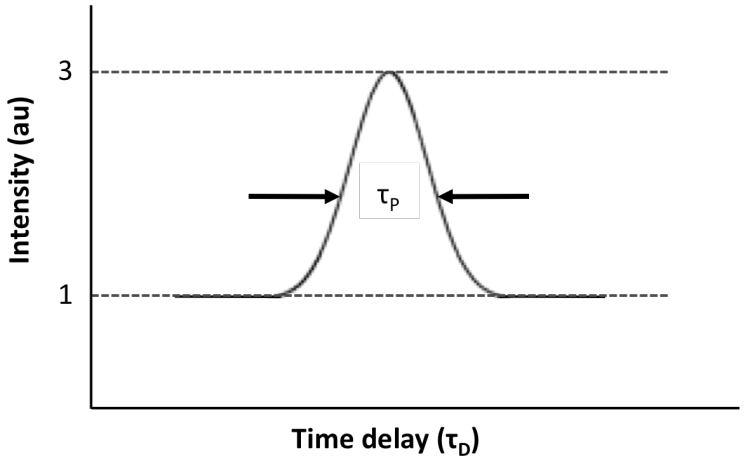

Figure B3: A typical autocorrelation trace of mode-locked pulses.

Here, τ_P is the FWHM of the autocorrelation trace. When it is divided by the factor of 1.55, the real pulsewidth is obtained in the case of $sech^2$ pulses.

VITA

M. Natali Çizmeciyan was born in Şişli, İstanbul on April 27, 1984. She received her BS degree in Physics from Marmara University in 2007. During her undergraduate studies, in 2005 and 2006, she also worked as a research assistant in the Laser Research Laboratory at Koç University. In 2007, she was admitted to the Master of Science program in Materials Science and Engineering at Koç University. Her research interests include mid-infrared solid-state lasers and spectroscopy of doped crystalline and glass materials. She will continue her Ph.D. work at Koç University in the same research area.

Publications:

- H. Kalaycioglu, H. Cankaya, M. N. Cizmeciyan, A. Sennaroglu, and G. Ozen, "Spectroscopic investigation of Tm^{3+}: TeO_2-WO_3 glass," Journal of Luminescence 128, 1501-1506 (2008).
- M. N. Cizmeciyan, H. Cankaya, A. Kurt and A. Sennaroglu, " Kerr-lens mode-locked femtosecond Cr^{2+}:ZnSe laser at 2420 nm" Optics Letters (submitted).

BIBLIOGRAPHY

[1] P. P. Sorokin and M. J. Stevenson, "Stimulated Infrared Emission from Trivalent Uranium," Physical Review Letters **5**, 557 (1960).

[2] Z. J. Kiss and R. C. Duncan Jr, "Pulsed and Continuous Optical Maser Action in CaF2:Dy2+," Proceedings of the IRE **50**, 1531-1532 (1962).

[3] L. F. Johnson, R. E. Dietz, and H. J. Guggenheim, "Optical Maser Oscillation from Ni2+ in MgF2 Involving Simultaneous Emission of Phonons," Physical Review Letters **11**, 318 (1963).

[4] L. F. Johnson, R. E. Dietz, and H. J. Guggenheim, "Spontaneous and stimulated emission from Co2+ ions in MgF2 and ZnF2," Applied Physics Letters **5**, 21-22 (1964).

[5] P. F. Moulton, A. Mooradian, and T. B. Reed, "Efficient cw optically pumped Ni:MgF2 laser," Optics Letters **3**, 164-166 (1978).

[6] L. D. DeLoach, R. H. Page, G. D. Wilke, S. A. Payne, and W. F. Krupke, "Transition metal-doped zinc chalcogenides: spectroscopy and laser demonstration of a new class of gain media," IEEE Journal of Quantum Electronics **32**, 885-895 (1996).

[7] R. H. Page, K. I. Schaffers, L. D. DeLoach, G. D. Wilke, F. D. Patel, J. B. TassanoJr., S. A. Payne, W. F. Krupke, K.-T. Chen, and A. Burger, "Cr^{2+} Doped Zinc Chalcogenides as Efficient, Widely Tunable Mid-Infrared Lasers," IEEE Journal of Quantum Electronics **33**, 609-619 (1997).

[8] K. L. Schepler, S. K¸ck, and L. Shiozawa, "Cr2+ emission spectroscopy in CdSe," Journal of Luminescence **72-74**, 116-117 (1997).

[9] J. McKay, K. L. Schepler, and G. C. Catella, "Efficient grating-tuned mid-infrared Cr2+:CdSe laser," Optics Letters **24**, 1575-1577 (1999).

[10] U. Hommerich, X. Wu, V. R. Davis, S. B. Trivedi, K. Grasza, R. J. Chen, and S. Kutcher, "Demonstration of room-temperature laser action at 2.5 μm from Cr2+:Cd0.85Mn0.15Te," Optics Letters **22**, 1180-1182 (1997).

[11] G. J. Wagner, T. J. Carrig, R. H. Page, K. I. Schaffers, J.-O. Ndap, X. Ma, and A. Burger, "Continuous-wave broadly tunable Cr2+:ZnSe laser," Optics Letters **24**, 19-21 (1999).

[12] U. Demirbas and A. Sennaroglu, "Intracavity-pumped Cr^{2+}: ZnSe laser with ultrabroad tuning range between 1880 and 3100 nm," Optics Letters **31**, 2293-2295 (2006).

[13] I. T. Sorokina, "Crystalline Mid-Infrared Lasers," in *Solid-State Mid-Infrared Laser Sources*, vol. 89, *Springer Topics in Applied Physics*, I. T. Sorokina and K. L. Vodopyanov, eds. (Springer, 2003) pp. 255-349.

[14] T. J. Carrig, G. J. Wagner, A. Sennaroglu, J. Y. Jeong, and C. R. Pollock, "Mode-locked Cr2+:ZnSe laser," Optics Letters **25**, 168-170 (2000).

[15] I. T. Sorokina, E. Sorokin, A. Lieto, M. Tonelli, R. H. Page, and K. Schaff, "Active and passive mode-locking of Cr2+:ZnSe laser," presented at Advanced Solid-State Lasers, 2001.

[16] C. R. Pollock, N. A. Brilliant, D. Gwin, T. J. Carrig, W. J. Alford, J. B. Heroux, W. I. Wang, I. Vurgaftman, and J. R. Meyer, "Mode locked and Q-switched Cr: ZnSe laser using a Semiconductor Saturable Absorbing Mirror (SESAM)," presented at Advanced Solid State Photonics, Vienna, Austria, 2005.

[17] H. A. Haus, "Mode-locking of lasers," Selected Topics in Quantum Electronics, IEEE Journal of **6**, 1173-1185 (2000).

[18] I. T. Sorokina, E. Sorokin, and T. J. Carrig, "Femtosecond pulse generation from a SESAM mode-locked Cr:ZnSe laser," presented at Lasers and Electro-Optics and 2006 Quantum Electronics and Laser Science Conference. CLEO/QELS 2006., 2006.

[19] A. V. Podlipensky, V. G. Shcherbitsky, N. V. Kuleshov, V. I. Levchenko, V. N. Yakimovich, M. Mond, E. Heumann, G. Huber, H. Kretschmann, and S. Kuck, "Efficient laser operation and continuous-wave diode pumping of Cr2+ :ZnSe single crystals," Applied Physics B: Lasers & Optics **72**, 253 (2001).

[20] C. Rablau, J. Ndap, X. Ma, A. Burger, and N. Giles, "Absorption and photoluminescence spectroscopy of diffusion-doped Cr2+:ZnSe," Journal of Electronic Materials **28**, 678-682 (1999).

[21] A. Burger, K. Chattopadhyay, J. O. Ndap, X. Ma, S. H. Morgan, C. I. Rablau, C. H. Su, S. Feth, R. H. Page, K. I. Schaffers, and S. A. Payne, "Preparation conditions of chromium doped ZnSe and their infrared luminescence properties," Journal of Crystal Growth **225**, 249-256 (2001).

[22] U. Demirbas, A. Sennaroglu, and M. Somer, "Synthesis and characterization of diffusion-doped Cr2+:ZnSe and Fe2+:ZnSe," Optical Materials **28**, 231-240 (2006).

[23] L. Pauling, *General Chemistry* (Dover, 1988).

[24] B. Henderson and G. F. Imbusch, *Optical Spectroscopy of Inorganic Solids* (Oxford University Press, 1989).

[25] H. A. Jahn and E. Teller, "Stability of Polyatomic Molecules in Degenerate Electronic States. I. Orbital Degeneracy," Proceedings of the Royal Society of London. Series A, Mathematical and Physical Sciences **161**, 220-235 (1937).

[26] J. T. Vallin, G. A. Slack, S. Roberts, and A. E. Hughes, "Infrared Absorption in Some II-VI Compounds Doped with Cr," Physical Review B **2**, 4313 (1970).

[27] A. Sennaroglu, U. Demirbas, N. Vermeulen, H. Ottevaere, and H. Thienpont, "Continuous-wave broadly tunable Cr2+:ZnSe laser pumped by a thulium fiber laser," Optics Communications **268**, 115-120 (2006).

[28] A. Gordon and F. X. Kartner, "Scaling of keV HHG photon yield with drive wavelength," Opt Express **13**, 2941-2947 (2005).

[29] V. Shcheslavskiy, F. Noack, V. Petrov, and N. Zhavoronkov, "Femtosecond Regenerative Amplification in Cr:Forsterite," Applied Optics **38**, 3294-3297 (1999).

[30] T. Udem, J. Reichert, R. Holzwarth, and T. W. H‰nsch, "Absolute Optical Frequency Measurement of the Cesium D1 Line with a Mode-Locked Laser," Physical Review Letters **82**, 3568 (1999).

[31] R. Holzwarth, T. Udem, T. W. H‰nsch, J. C. Knight, W. J. Wadsworth, and P. S. J. Russell, "Optical Frequency Synthesizer for Precision Spectroscopy," Physical Review Letters **85**, 2264 (2000).

[32] E. Sorokin, I. T. Sorokina, J. Mandon, G. Guelachvili, and N. Picque, "Sensitive multiplex spectroscopy in the molecular fingerprint 2.4 μm region with a Cr2+:ZnSe femtosecond laser," Opt Express **15**, 16540-16545 (2007).

[33] J. Mandon, E. Sorokin, I. T. Sorokina, G. Guelachvili, and N. PicquÈ, "Supercontinua for high-resolution absorption multiplex infrared spectroscopy," Optics Letters **33**, 285-287 (2008).

[34] W. S. Pelouch, G. J. Wagner, and T. J. Carrig, "Mid-Wave ZGP OPOs Pumped by a Cr:ZnSe Laser," presented at Advanced Solid-State Lasers, 2001.

[35] I. T. McKinnie, G. J. Wagner, S. Christensen, T. J. Carrig, and C. B. Rawle, "Dual-band mid-wave/long-wave ZGP OPO pump-tuned by a Cr:ZnSe laser," presented at Lasers and Electro-Optics, 2002. CLEO '02. Technical Digest. Summaries of Papers Presented at the, 2002.

[36] P. F. Moulton, "An Investigation of the Co:MgF_2 Laser System," IEEE Journal of Quantum Electronics **21**, 1582-1595 (1985).

[37] O. E. Martinez, R. L. Fork, and J. P. Gordon, "Theory of passively mode-locked lasers including self-phase modulation and group-velocity dispersion," Optics Letters **9**, 156-158 (1984).

[38] M. Bass, *Handbook of Optics*, vol. 2, 2 ed (McGraw-Hill, 1994).

[39] R. L. Fork, C. H. B. Cruz, P. C. Becker, and C. V. Shank, "Compression of optical pulses to six femtoseconds by using cubic phase compensation," Optics Letters **12**, 483-485 (1987).

[40] S. M. J. Kelly, "Characteristic sideband instability of periodically amplified average soliton," Electronics Letters **28**, 806-807 (1992).

[41] H. A. Haus, "Mode-Locking of Lasers," Ieee J Quantum Elect **6**, 1173-1185 (2000).

[42] I. T. Sorokina and K. L. Vodopyanov, *Solid-State Mid-Infrared Laser Sources*, vol. 89 (Springer).

[43] R. A. Kaindl, M. Wurm, K. Reimann, P. Hamm, A. M. Weiner, and M. Woerner, "Generation, shaping, and characterization of intense femtosecond pulses tunable from 3 to 20 mu m," Journal of the Optical Society of America B-Optical Physics **17**, 2086-2094 (2000).

[44] J.-C. Diels and W. Rudolph, *Ultrashort Laser Pulse Phenomena*, 2 ed (Elsevier, 2006).

[45] A. Yariv, *Optical Electronics in Modern Communications*, Fifth Edition ed (Oxford University Press, 1997).